An Atomistic-Based Hierarchical Multiscale Examination of Age Hardening in an Al-Cu Alloy

CHANDRA VEER SINGH and DEREK H. WARNER

A large class of modern structural alloys derives its strength from precipitation hardening. Precipitates obstruct the motion of dislocations and thereby increase alloy strength. This paper examines the process using an atomistic-based hierarchical multiscale modeling framework. Atomistic modeling is employed to (1) compute solute-dislocation interaction energies for input into a semi-analytic solute hardening model and (2) evaluate precipitate strengths for use in dislocation line tension simulations. The precipitate microstructure in the dislocation line tension simulations is obtained from simple analytic precipitation kinetics relations. Fitting only the rate constants in the precipitation kinetics model, the macroscopic strength predictions of the hierarchical multiscale model are found to correspond reasonably well with experiments. By analyzing the potential sources of discrepancy between the model's macroscopic predictions and experiments, this work illuminates the importance of specific atomic-scale processes and highlights important challenges that remain before truly predictive mechanism-based plasticity modeling can be realized.

I. INTRODUCTION

NEAR the beginning of the 20th century, Alfred Wilm[1] discovered that the hardness of quenched Al alloys evolves in time. While Wilm's discovery laid the foundation for many modern engineering alloys, the phenomenon had already been inadvertently utilized by the Wright brothers during their historic flight of 1903.[2] In the 50 years following Wilm's discovery, the evolving hardness in Al alloys was linked to an evolving microstructure, thanks to advancements in dislocation theory[3–5] and the observation of nanometer-sized solute clusters by X-ray scattering[6,7] and transmission electron microscopy (TEM).[8] In the last 50 years, utilization of this phenomenon, now known broadly as precipitation hardening, has consistently progressed,[9,10] with the most recent precipitation hardened Al alloys demonstrating strengths approaching 1 GPa while maintaining significant ductility.[11,12]

In Al-Cu alloys, the evolution of the microstructure at common aging temperatures [383 K (110 °C) to 423 K (150 °C)] and Cu concentrations (~4 wt pct Cu) consists of[13] SSSα → GP zones → θ'' (GP2 zones) → $\theta' \to \theta$ (CuAl$_2$) with SSSα representing a supersaturated solid solution and GP zones being nanometer-sized Cu disk-shaped monolayers on {100} planes. θ'' precipitates are larger than GP zones and consist of two disk-shaped Cu monolayers on {100} planes separated by three planes of Al atoms. θ' precipitates are Al$_2$Cu platelets having a tetragonal structure. θ precipitates constitute the equilibrium precipitate phase with Al$_2$Cu stoichiometry and body-centered tetragonal structure. GP zones and θ'' precipitates are fully coherent with the Al matrix, θ' is semi-coherent, and θ is incoherent. Although multilayer GP zones have been observed,[14] there is a general agreement that they are a single atomic layer thick.[15] The Cu content of GP zones, however, has not been settled with different experimental observations showing significant variation from 40 to 100 pct[14,16] with an average value of about 80 pct.[16]

The presence of precipitates restricts the motion of dislocations and thus affects macroscopic strength. During the initial stages of age hardening, precipitate size and volume fraction increase, leading to an increase in strength. However, in the later stages, precipitates grow at the expense of others, leading to an increase in precipitate spacing and a decrease in strength. In binary Al-Cu alloys, optimum strength typically occurs near the transition from θ'' precipitates to θ' precipitates.[17]

A variety of dislocation–precipitate interaction mechanisms have been proposed in the literature on the subject. Elastic interactions between a dislocation and a precipitate arise in two ways: misfit stresses associated with the difference in lattice constants between the precipitate and the matrix[18,19] and the difference in elastic modulus between the precipitate and the matrix.[20,21] Inelastic chemical interactions are also often cited to play an important role. A dislocation will have a different core energy when in a precipitate compared to the matrix.[22] Additionally, a ledge must be formed at the surface of a precipitate when a dislocation enters and leaves it.[23] Experimental efforts to illuminate the relative importance of these mechanisms have not provided a clear consensus.[24–28]

CHANDRA VEER SINGH, Assistant Professor, is with the Department of Materials Science and Engineering, University of Toronto, 184 College St., Toronto, ON M5S 3E4, Canada. DEREK H. WARNER, Assistant Professor, is with the School of Civil and Environmental Engineering, Cornell University, Ithaca, NY 14853. Contact e-mail: dhw52@cornell.edu
Manuscript submitted April 16, 2012.
Article published online February 14, 2013.

Atomistic simulations hold great promise for providing insight into the importance of dislocation–precipitate interaction mechanisms, especially considering that algorithms, methods, and computational resources continue to improve. Some notable examples of simulations where dislocation interactions with precipitates and other material defects have been studied include[29–31] interactions with grain boundaries,[32] interactions with interfaces and resulting ductility and strain rate sensitivity in nano-twinned copper,[33–35] interactions with voids and copper precipitates in α-iron in radiation environment,[36–39] interactions with precipitates in other alloys, and[40] a comprehensive review of dislocation obstacle interactions at the atomic level including solutes, voids, precipitates, and obstacles with dislocation character such as dislocation loops and stacking fault tetrahedra. An emerging theme from these studies is the staggering complexity of dislocation-defect interactions. Thus, while continuum dislocation theory is an invaluable tool for understanding dislocation behavior within a generalized context, the complexity of dislocation-defect interactions often warrants an atomistic analysis. Nonetheless, atomistic modeling comes with its own set of challenges when trying to connect with reality, such as its limited spatial and temporal domains and the challenge of accurately and feasibly computing interatomic forces.

Current materials design approaches for precipitation hardened alloys are based on empirical continuum theories that do not include many of the complexities of dislocation-precipitate interactions.[41–43] Correspondingly, a primary objective of this work is to examine precipitate strengthening starting from atomistic-based modeling. To link our atomic-scale results to macroscopic behavior, we utilize discrete dislocation line tension modeling and simple precipitation kinetics modeling. By combining these modeling methodologies into a single hierarchical multiscale framework, the predictive capabilities of each component can be better assessed, illuminating key challenges that remain with regard to mechanism-based plasticity modeling.

This manuscript begins with the discussion of atomistic-based modeling of dislocation–precipitate and dislocation–solute interactions. Then, a continuum dislocation line tension model is developed for assessing the collective effects of dislocation–precipitate interactions, followed by the analytic precipitation kinetics model. Subsequently, age hardening predictions are presented along with parametric studies of the effects of aging temperature and Cu concentration. These strength predictions are made without including the effects of thermal activation during mechanical testing and thus are significantly higher than experimental strengths. In the final section of the paper, the influence of thermal activation is considered, providing a more direct comparison with experiments.

II. PRECIPITATION HARDENING

Dislocation-precipitate interactions are very complex. Even if the scope is restricted to nanometer-sized, plate-shaped precipitates in a binary Al-Cu alloy, a multitude of parameters can affect the mechanism by which a dislocation overcomes a precipitate and the associated critical resolved shear stress (τ_c). Key parameters include (a) dislocation–precipitate orientation, (b) precipitate size, (c) the location at which the slip plane of the dislocation intersects the precipitate (offset), (d) the influence of neighboring precipitates, (e) temperature, (f) dislocation character, (g) previous dislocation–precipitate interactions, and (h) strain rate/time scale. While a complete study of all these parameters and their cross interactions is unfeasible, the role of each parameter is discussed here to some degree. However, for this paper to remain true to its focus on age hardening, the reader will be referred to other work for a detailed description in some cases, e.g., only edge dislocations are considered in this manuscript. A study of screw dislocation interactions with GP zones can be found in Singh et al.[39] Additionally, we have limited our study to dislocation interactions with GP zones and θ'' precipitates. The larger θ' and θ precipitates are not currently accessible to atomistic simulation; however, due to the fact that they are impenetrable to dislocations, their interaction with dislocations is likely amenable to simple continuum treatment. The atomistic simulation details are provided in Appendix A.

A. GP Zone Strengthening

Traditional wisdom suggests that dislocations overcome precipitates either by cutting or by Orowan looping.[44,45] Our atomistic simulations of dislocation-GP zone interactions display both of these mechanisms and variations of the two, dependent upon the specific parameters of the interaction. Figure 1 shows two cases of edge dislocation interacting with GP zones of 4.4 nm diameter at 0 K where the slip plane of the dislocation intersects the center point of the GP zone, i.e., offset = 0. Movies of these two interactions are provided in the online supplementary material. In order to visualize the interaction, we only plot the atoms not in perfect FCC stacking, i.e., having a large "centro-symmetry parameter,"[46] using the AtomEye visualization software.[47] For the 60 deg interaction (Figure 1(a)), the leading partial dislocation cuts the GP zone, while the trailing partial loops around it. The Orowan looping of the trailing partial is the critical event controlling τ_c. For 60 deg interactions with smaller GP zones (diameter<3 nm), both partial dislocations overcome the GP zone via precipitate cutting. On the other hand, in the case of the 0 deg interaction (Figure 1(b)), the edge dislocation overcomes the precipitate by full Orowan looping. This mechanism has been observed across all GP zone sizes that have been investigated for the 0 deg interaction. As reported previously,[38] the offset between the dislocation glide plane and the GP zone center can significantly influence the interaction mechanism, e.g., diffusionless climb and defect nucleation at the dislocation-GP zone contact point have also been observed at high offsets.

To make the atomistic simulation-based precipitation hardening predictions performed here computationally
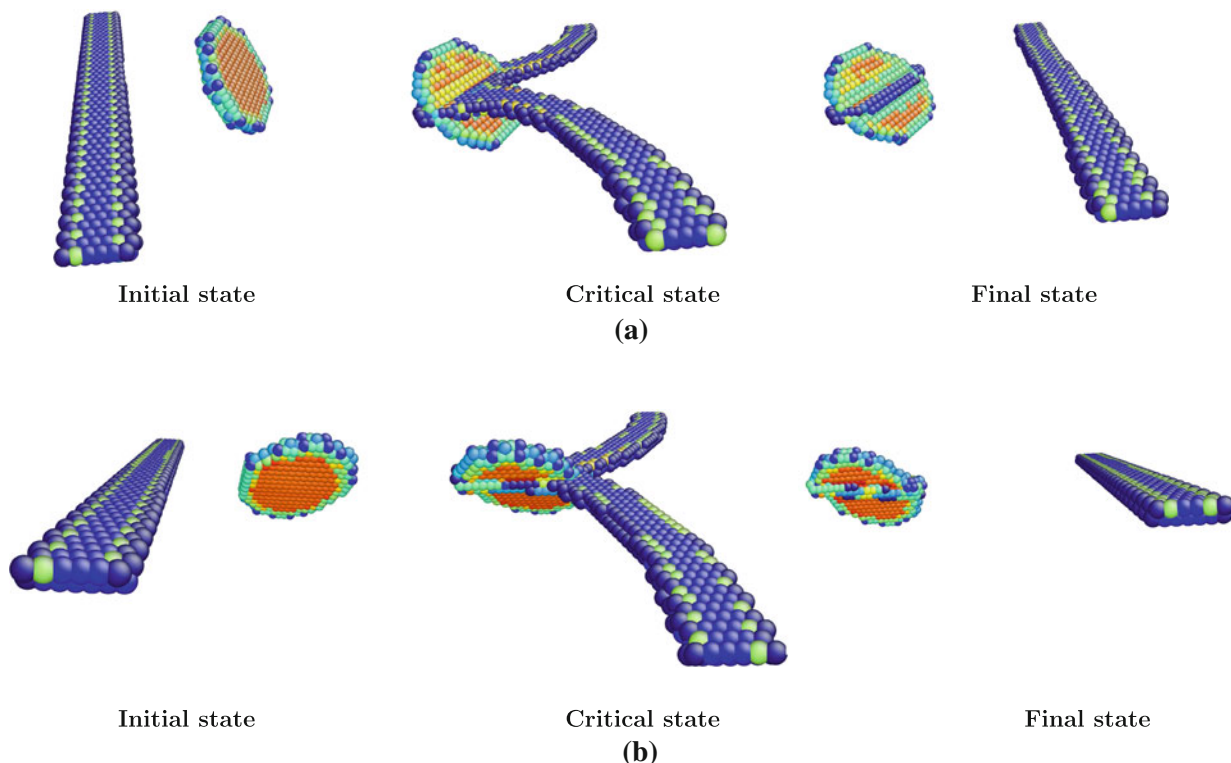
Fig. 1—Dominant mechanisms by which an edge dislocation overcomes GP zones: (a) 60 deg interaction involving leading partial cutting and trailing partial looping, (b) 0 deg interaction involving full dislocation looping. Movies of the dislocation-GP zone interaction are provided in the supplementary online material.

feasible, we have limited the modeling to edge dislocation interactions. The role of dislocation character has been examined in detail in our earlier report.[39] For screw dislocation-GP zone interactions, the 60 deg orientation yields two prevalent mechanisms depending upon offset. The first involves full Orowan looping, similar to the 0 deg edge dislocation interaction described above. The second entails the screw dislocation cross-slipping onto a plane that allows it to glide past the GP zone without intersecting it. Cross-slip was observed at both 0 K and finite temperatures, indicating that it can be an important mechanism even in the absence of thermal activation. For the 0 deg interaction involving a screw dislocation, cross-slip was also observed. However, the plane onto which the dislocation cross-slips is also impeded by the GP zone. In this case, the cross-slip mechanism leads to an enhancement of precipitate strengthening.[39]

A key parameter that affects τ_c is the spacing between neighboring precipitates along the dislocation line. The most common approach for incorporating the effect of spacing involves two assumptions: (1) the precipitate spacing, L, is much larger than both the precipitate diameter, D, and the dislocation core width; and (2) the applied force acting to move the dislocation forward at the precipitate results solely from its line tension and configuration. These assumptions provide a one-to-one relationship between the precipitate's ability to inhibit dislocation glide (precipitate strength) and the configuration of the dislocation just before it overcomes the precipitate, described by its critical bowing angle, ϕ_c. Different analytic relations for τ_c based on the dislocation line tension model are described in Appendix B. These include (i) Friedel's shear cutting relation,[48] (ii) Orowan looping,[49] (iii) Orowan relation modified to include finite D/L ratio,[26] and (iv) Scattergood-Bacon relation that includes dislocation self-interactions.[50]

Figure 2 reports τ_c values measured from atomistic simulations having various cell dimensions in Z, equivalent to different GP zone spacings, L. The simulation results correspond to the 60 deg edge dislocation-GP zone interaction with a 4.4 nm diameter GP zone at 0 K. We find that the data for $L \gg D$ can be well described by both the simple $\tau_c \propto 1/L$ relation and the Scattergood and Bacon relation, Eq. [B4]. It is interesting to note that for $L/D < 2$, the $1/L$ rule does better than the Scattergood & Bacon relation, and the $\tau_c \propto 1/(L - D_p)$ relation does not seem to work at all (here $D_p = D \cos(30 \deg)$). For the former relation, ϕ_c was considered a fitting parameter with $G = 31.6$ GPa and $b = 2.86$ Å, while for the latter, B was fit to 2.89. For the $\tau_c \propto 1/L$ relation, ϕ_c was fit as 132 deg, which compares well with the maximum bowing angle observed in the simulations (Figure 1(a)). In the spirit of Eq. [B3], we find that a particularly good fit is given by the relation $\tau_c \propto 1/(L - a_1 D)$ with $a_1 = 0.19$ and $\phi_c = 134$ deg. Based on these observations, particularly the utility of the simple $\tau_c \propto 1/L$ model down to small precipitate spacing relative to precipitate diameters, $L/D \approx 1$, $\tau_c \propto 1/L$ is used in the subsequent analysis.
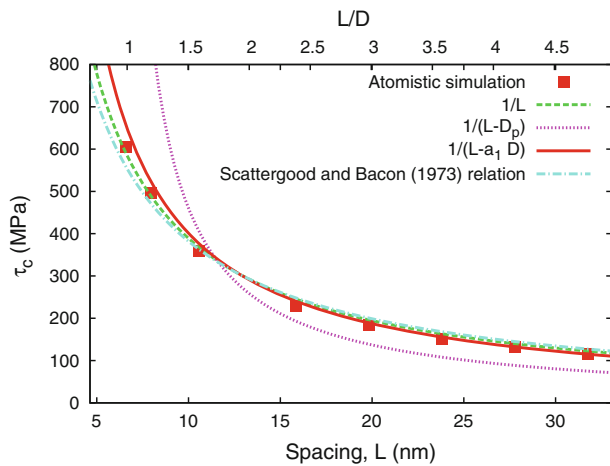
Fig. 2—Resolved shear stress required for an edge dislocation to overcome a periodic array of equally spaced 4.4 nm GP zones at 0 K (−273 °C) (60 deg interaction) as a function of GP zone spacing. Solid lines show several popular analytic models which were fit to the atomistic data.
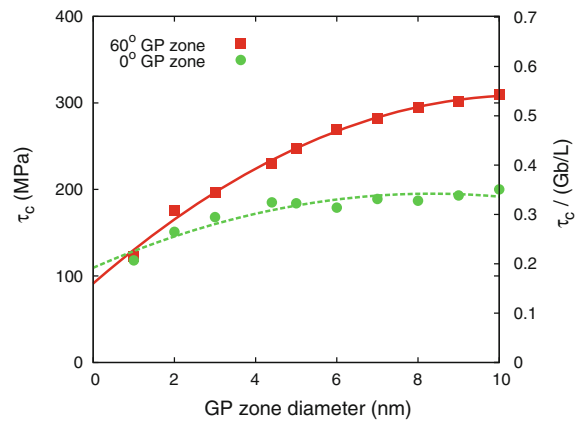

Fig. 3—Resolved shear stress required for an edge dislocation to overcome a periodic array of equally spaced GP zones at 0 K (−273 °C) as a function of GP zone diameter. The atomistic simulation data, corresponding to $L = 15.9$ nm, are described by phenomenological fits, $i.e.$, $\tau_c = -1.92D^2 + 40.85D + 91.27$ for the 60 deg interaction and $\tau_c = -1.23D^2 + 20.55D + 109.42$ for the 0 deg interaction.

τ_c is also controlled by the precipitate size. Figure 3 reports τ_c from simulations involving edge dislocations interacting with GP zones at 0 K with a simulation cell depth (spacing between GP zones centers) of $L = 15.9$ nm. In all cases, the slip plane of the dislocation intersects the center of the GP zone. We note that while the values of τ_c reported in Figure 3 correspond to $L = 15.9$ nm, larger simulation cells were used for the largest GP zone sizes ($D > 6$ nm) to insure sufficient spacing between periodic GP zone images. In these cases, τ_c values were then scaled to $L = 15.9$ nm using $\tau_c \propto 1/L$. For 60 deg interactions, the simulations suggest that strength increases linearly with GP zone diameter for small- to medium-sized GP zones, but asymptotically saturates as the diameter becomes large ($D > 8$ nm). Considering that τ_c is controlled by Orowan looping of the trailing partial for the 60 deg interaction when the GP zone diameter is greater than 3 nm, we attribute the size dependence to the attractive interaction between the neighboring segments of the bowed-out dislocation. Following the $(1/r)$ stress field associated with a dislocation, the attractive interaction between the neighboring bowed-out dislocation segments is a decaying function of the distance between the segments, which scales with the diameter of the GP zone. We note that traditional chemical hardening arguments for dislocation-precipitate interactions would suggest a linear size dependence for this orientation, inconsistent with the behavior reported here. Also, the chemical hardening models are not consistent with the cutting mechanism that we observe, $i.e.$, a zipping motion of the dislocation across the face of the GP zone, which would not yield a linear size dependence. τ_c for 0 deg interactions is generally smaller and exhibits a smaller dependence on GP zone diameter. This is consistent with the interaction geometry and mechanism of Orowan looping since the precipitate diameter does not influence the dislocation in its bowed-out state. The maximum values of τ_c from our simulations are $0.35\,\tau_c^{Orowan}$ for the 0

deg interaction and $0.55\,\tau_c^{Orowan}$ for the 60 deg interaction, where $\tau_c^{Orowan} = 570$ MPa for this box size.

The location at which a dislocation intersects the GP zone relative to its center (offset) has been observed to substantially influence τ_c for a particular interaction.[38] Building from our previous work and ignoring the special cases of defect generation and diffusionless climb, we include the effect of offset into our dislocation line tension model as $\tau_c(O) = \tau_{c0} + O\delta\tau_c$. τ_{c0} represents τ_c when the dislocation intersects the GP zone through its center. O represents the offset, $i.e.$, the location of the active slip plane relative to the center of the GP zone, normalized with respect to the {111} interplanar spacing distance. Based on our previous work,[38] the offset effect is taken as $\delta\tau_c = 0.012\tau_c^{Orowan}$ and $0.015\tau_c^{Orowan}$ for 60 and 0 deg dislocation-GP zone interactions, respectively. Finally, we point out that successive dislocation-GP zone interactions are ignored in this work. We direct the interested reader to[38] where the complexity of successive interactions is documented.

B. θ'' Strengthening

As mentioned previously, θ'' precipitates are modeled as two layers of Cu atoms separated by three atomic layers of Al. Figure 4 depicts the mechanism by which they are overcome by edge dislocations at 0 K (−273 °C) for all diameters studied here, 8 to 30 nm. For the 60 deg interaction, the Cu atoms are displaced by a partial burgers vector after the dislocation overcomes the precipitate. In this regard, the interaction is similar to that observed for the 60 deg edge dislocation interactions with large GP zones (Figure 1(a)). However, in the case of the GP zone, the leading partial clearly cuts the GP zone before the critical state, whereas the leading partial does not cut the θ'' precipitate before the critical state. Thus, the 60 deg θ'' mechanism could entail full Orowan looping at the critical state with the leading partial component of the full dislocation loop collapsing
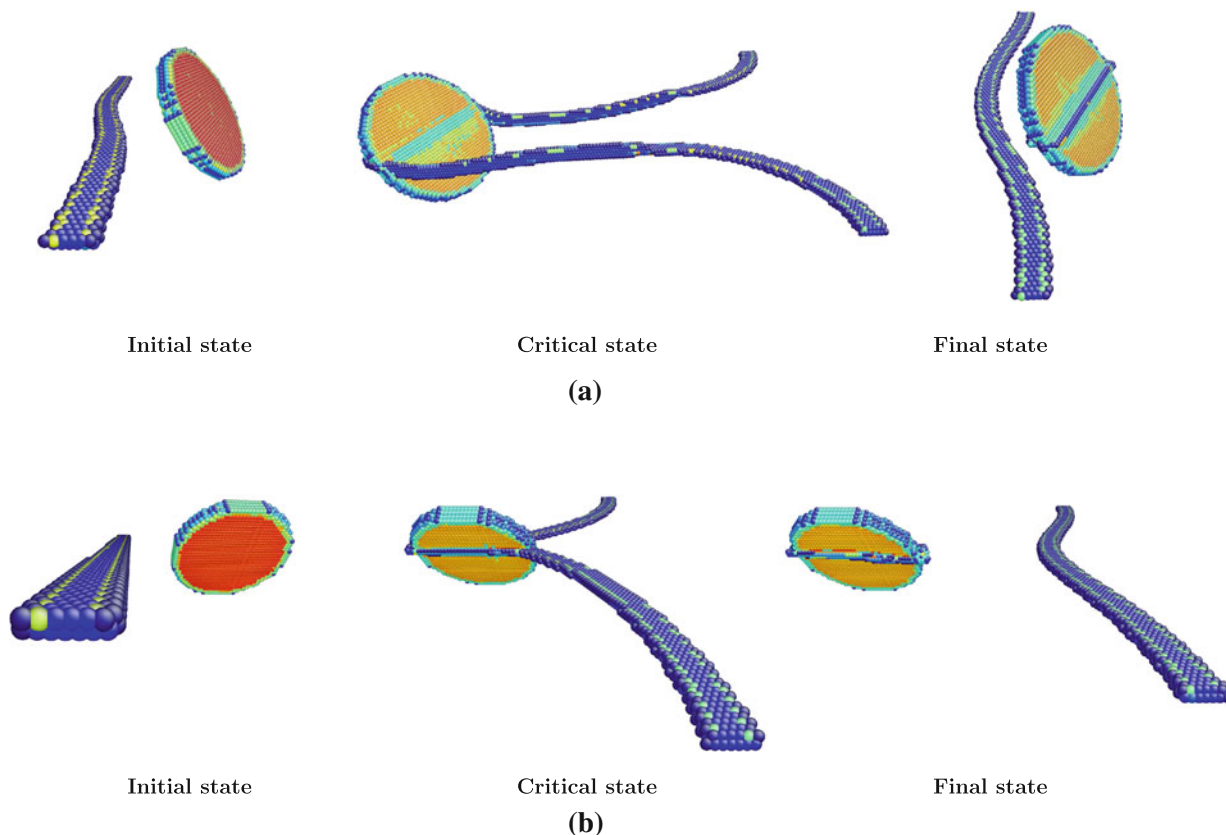
Initial state   Critical state   Final state

(a)

Initial state   Critical state   Final state

(b)

Fig. 4—Dominant mechanisms by which an edge dislocation overcomes θ'' precipitates: (*a*) 60 deg interaction involving leading partial cutting and trailing partial looping, note the cross-slipped segments of the dislocation in the critical state, (*b*) 0 deg interaction involving full dislocation looping.

through the θ'' precipitate after it is formed. Or, alternatively, leading partial cutting may occur. The critical state of the 60 deg θ'' dislocation interaction involves a completely bowed-out dislocation where the screw segments of the bowed dislocation have cross-slipped. The cross-slip of the screw segments of a bowed edge dislocation at a precipitate was first envisioned by Hirsch[51] and has been more recently observed in atomistic simulations of impenetrable precipitates in Cu.[52] Here, the cross-slipped segments of the dislocation are observed to cross-slip back to their original plane as the dislocation overcomes the precipitate, making the later stages of the mechanism observed here distinctly different than the Hirsch mechanism.[51,53] It is also worth noting that the cross-slip observed in our simulations takes place at 0 K, in the absence of thermal activation. The 0 deg interaction exhibits full Orowan looping for all sizes studied (8 to 16 nm), Figure 4(b), analogous to the 0 deg edge dislocation-GP zone interaction. Interestingly, these results viewed as a whole suggest that for plate-shaped precipitates, the competition between Orowan looping and cutting mechanisms may be more influenced by orientation than the precipitate size, at least in the athermal limit.

τ_c as a function of θ'' precipitate diameter is shown in Figure 5 for both the 60 and 0 deg interaction orientations. θ'' diameters spanning 8 to 30 nm for the 60 deg interaction and 8 to 16 nm for the 0 deg interaction were
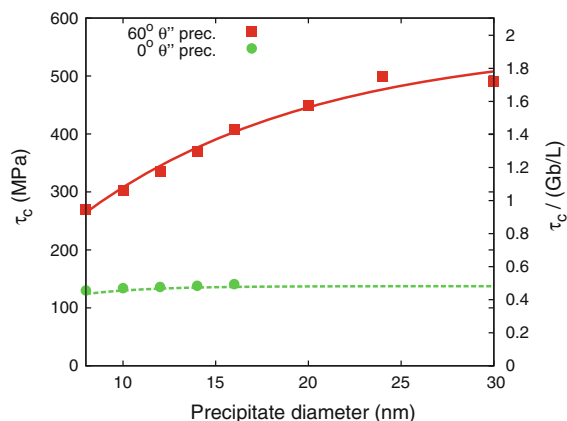

Fig. 5—Resolved shear stress required for an edge dislocation to overcome a periodic array of equally spaced θ'' precipitates at 0 K (-273 °C) as a function of their diameter. The atomistic simulation data, corresponding to $L = 31.8$ nm, are described by phenomenological fits, *i.e.*, $\tau_c = 558.36\,(1 - exp(-0.08D))$ for the 60 deg interaction and $\tau_c = 137.40\,(1 - exp(-0.29D))$ for the 0 deg interaction.

investigated. The minimum simulation cell size for these studies was approximately $34 \times 42 \times 32$ nm^3 and it was increased for larger precipitates. In Figure 5, the simulation results are normalized to $L = 31.8$ using $\tau_c \propto 1/L$. In all cases, the θ'' precipitate provides significantly

greater strengthening than GP zones, with maximum values of $\tau_c/\tau_c^{Orowan} = 1.754$ and $\tau_c/\tau_c^{Orowan} = 0.495$ for the 60 and 0 deg orientations, respectively. The most notable feature of the results is the super-Orowan strengthening associated with the 60 deg interaction. This can be attributed to the controlling mechanism of this interaction, *i.e.*, the cross-slip of the screw dislocation segments back onto their original slip plane. While the size of simulation cell prohibited an extensive finite temperature investigation of this occurrence, experience with cross-slip strengthening of screw dislocation-GP zone interactions[39] suggests that thermal activation can significantly reduce the stress at which the second controlling cross-slip event occurs. Thus, the high values of τ_c of the 60 deg to θ'' interaction cited here may not be representative of behavior at typical experimental time scales and temperatures.

Orientation has a significant effect on τ_c for the dislocation-θ'' precipitate interactions. τ_c for the 0 deg interactions is relatively insensitive to precipitate size, while τ_c for the 60 deg precipitate interactions approximately doubles as diameter increases from 8 to 30 nm. While the size independence of the 0 deg interaction can easily be attributed to the controlling mechanism, the behavior of the 60 deg interaction is not as easily understood. For θ'' precipitates, the effect of offset on τ_c is unknown. Thus, we assume the effect is similar to what we have observed for the GP zone interactions and incorporate its effect in an identical manner.

III. SOLUTE HARDENING

A. Methodology

To model solute hardening in Al-Cu, we have utilized a semi-analytic method recently developed by Leyson et al.[54] The method stems from the framework developed by Labusch[55,56] for understanding solute hardening from the perspective of dislocation glide being inhibited by the heterogeneous energy landscape that a dislocation encounters in a field of randomly positioned solute atoms. Relying on input from atomistic simulation, both elastic and chemical contributions to solute hardening are included with no adjustable parameters. For brevity, the key components of the model are presented in the Appendix C and the reader can refer to Leyson et al.[54] for the full derivation. Accordingly, the shear stress needed to move a typical segment of dislocation forward through an array of randomly distributed solute atoms, in the athermal limit, is given by

$$\tau_{ys} = \frac{\pi}{2} \frac{\Delta E_b}{b \xi_c w_c} \qquad [1]$$

where ΔE_b represents the energy barrier to the dislocation glide posed by solute atoms, and ξ_c and w_c signify the dislocation segment length and the incremental glide distance of a dislocation segment in a field of solute atoms, respectively. w_c is taken to be the splitting distance of the dislocation core, which was found in Leyson et al.[54] to correspond to the most energetically favorable choice. ΔE_b is in turn a function of the interaction energy between a dislocation and Cu solute

atoms, ΔE_p (see Appendix C for details). Noting that both ξ_c and ΔE_b are functions of c_s, Eq. [1] can be rewritten[54] to show that $\tau_{ys} \propto c_s^{2/3}$, consistent with the experimental data.

As with the precipitation hardening simulations, the newly developed Al-Cu angular-dependent EAM interatomic potential[57] was used to compute interaction energy between dislocation and Cu solute at different lattice sites. A simulation cell of $11 \times 11 \times 10$ nm^3 with 69,320 atoms and an edge dislocation at its center was utilized. Following,[58] the atoms in several $X - Y$ planes around $Z = 0$ were held fixed to prevent the dislocation from freely moving toward (or away from) the Cu atom.

B. Predictions

The interaction energy, ΔE_p, as a function of Cu solute position is shown in Figure 6. In the figure, unfilled circles represent the lattice sites at which the interaction energies were calculated. Away from the dislocation core, the interaction energies correspond well with the continuum linear elasticity solution, which is based on the interaction energy of the hydrostatic stress fields. Near the dislocation core, where the interaction energies are the strongest, they were found to range between −0.15 and 0.25 eV.

Using Eq. [1], $\tau_{ys}/c_s^{2/3}$ is found to be 1138 MPa. This is about 2.5 times the value reported by Leyson et al.[54] who used interaction energies calculated from Kohn-Sham density functional theory (DFT). We attribute the large difference in the interaction energies to a difference in the atomic misfit volume and subsequently the dilute heat of solution. Specifically, the misfit volume of a substitutional Cu atom in an Al lattice with the Al-Cu potential used here is −7.5 Å^3, whereas DFT predicts a value of −5.6 Å^3. Considering that the strain energy associated with the misfit volume is a significant contributor to the dilute heat of solution of Cu in Al,
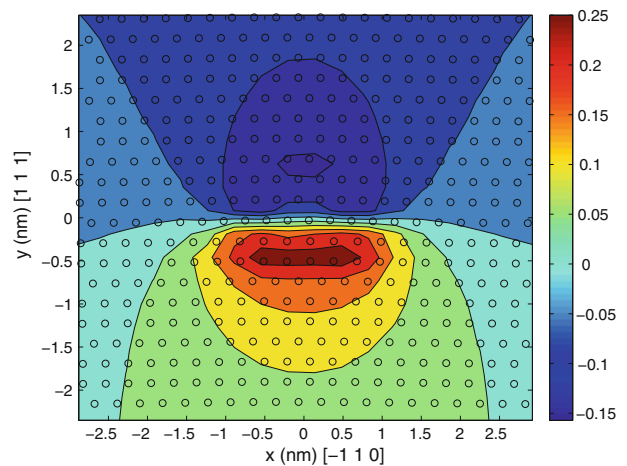

Fig. 6—The interaction energy between dilute Cu solute atoms and an edge dislocation lying on the *xy* plane and centered about (0,0). Contour colors are in eV and were calculated *via* atomistic simulation at the lattice sites (unfilled circles).

the dilute heat of solution shows a similar trend, *i.e.*, −0.1807 eV for the Al-Cu potential used here, −0.08 eV from DFT, and −0.14 eV from the CALPHAD database.[59] A comparison with experiments[60,61] suggests that the true value of $\tau_{ys}/c_s^{2/3}$ is between the DFT prediction and our own empirical potential-based prediction, and likely much closer to the DFT value. However, the results of[17] do clearly show a stronger strength dependence, $\tau_{ys}/c_s^{2/3}$, on solute concentration than the DFT prediction, indicative of the challenge associated with predicting solute hardening.

Another potential source of error in our calculation of τ_{ys} is the choice of w_c, which we chose to match the splitting distance of the dislocation core, 1.0 nm. Because this choice is somewhat flexible in nature,[54] we have examined the dependence of τ_{ys} on w_c. Upon increasing w_c, ΔE_b increases and τ_{ys} decreases. For w_c varying from 0.8 nm to 1.4 nm, ΔE_b increases from 2.13 eV to 4.09 eV. This reduces τ_{ys} to 923 MPa at $w_c = 0.8$ nm from 1346 MPa at $w_c = 1.4$ nm. In addition to bounding the error, these results indicate the importance of the dislocation core splitting distance, a characteristic that often varies between material models, *e.g.*, DFT and empirical potentials.

The critical shear stress at which a dislocation moves through a field of randomly positioned solute atoms, τ_{ys}, can, in principle, be computed directly from mechanically loaded atomistic simulations.[58] Such calculations are computationally expensive due to the sensitivity of τ_{ys} on the random positions of the solute atoms in the limited spatial dimensions accessible to atomistic simulation. This requires many realizations of solute fields to obtain τ_{ys} to a reasonable precision. Initially, we planned to compute τ_{ys} in this way. The effort began with a validation of the mechanically loaded simulation setup by reproducing previously published results involving Al-Mg solute hardening.[58] Then, Al-Cu solute hardening was examined. However, in the Al-Cu case, erroneously large strengths were obtained, $\tau_{ys}/c_s^{2/3} = 8{,}520$ MPa. This motivated us to use the semi-analytic model presented in this section. Considering that the semi-analytic model provides more reasonable results, the high value of τ_{ys} measured from direct simulations can be attributed to a feature of the Al-Cu potential not included in the semi-analytic model, such as non-equilibrium state energetics, *e.g.*, bond breaking energetics.

In summary, the solute hardening work performed here emphasizes two points. The first is that the misfit volume and heat of solution are important fitting parameters when designing an interatomic potential that can accurately predict solute hardening, noting that this point is generally consistent with traditional wisdom. The second is that characteristics beyond misfit volume and heat of solution can also significantly affect solute hardening, as made evident when comparing direct simulation results with the semi-analytic model. With respect to the ultimate goal of this work, atomistic-based age hardening predictions, we will use the results obtained from the semi-analytic modeling of τ_{ys}, while remaining cognizant of shortfalls of the Al-Cu potential identified here.

IV. MACROSCOPIC STRENGTH MODELING

While τ_{ys} represents the critical resolved shear stress (CRSS) for a dislocation to propagate through a field of randomly positioned solute atoms, τ_{c_i} represents the CRSS for a dislocation to overcome a periodic array of identical precipitates (the subscript i has been added to the value previously referred to as τ_c to denote the instance corresponding to a specific precipitate type, size, orientation, offset, and spacing). Accordingly, a precipitation strengthening contribution more relevant to a real material is the CRSS required for a dislocation to propagate through a field of precipitates with different types, sizes, orientations, offsets, and random positions, τ_{yp}. Here, we use a discrete dislocation model governed by continuum line tension mechanics[48] to compute τ_{yp}. Taking as input τ_{c_i}'s from the atomistic simulations, τ_{yp} is then the value of CRSS at which a dislocation traverses a field of precipitates in the discrete dislocation model. The discrete dislocation model is used to generate a set of τ_{yp} values corresponding to different time points during age hardening. To generate continuous aging curves, the values generated at discrete time points from the discrete dislocation model are interpolated using a standard analytic model with a single fitting parameter. Keeping the fitting parameter constant, we then examine the effects of Cu concentration, aging temperature, and the role of thermal activation during mechanical testing.

The continuum line tension–discrete dislocation modeling performed here is based on the algorithm originally devised by[62] and most recently employed for point obstacles by.[63–65] Briefly, the algorithm consists of representing a dislocation line in a field of precipitates by a series of circular segments connecting the precipitates that the dislocation is in contact with. The segments have a circular radius of curvature, $R = \frac{Gb}{2\tau_{app}}$, that is a function of the applied resolved shear stress, τ_{app} (Figure 7). As τ_{app} is increased, the dislocation segments bow further and can come in contact with other precipitates, creating two segments out of one. The propagation of the dislocation line is controlled by its detachment from precipitates. This occurs when one of two conditions are met: (1) a precipitate is connected to a segment that has a radius of curvature less than half the distance between the two precipitates to which it is attached, *i.e.*, a segment of the dislocation becomes mechanical unstable, or (2) the angle at which a dislocation segment(s) connects to a precipitate reaches a critical value.

The critical bowing angle, ϕ_{c_i}, is the means by which the strength, τ_{c_i}, of a specific dislocation-precipitate interaction, i, measured in atomistic simulation is provided as an input into the discrete dislocation model. We note that while dislocation self-interaction is not explicitly included in the continuum line tension model, the effect is implicitly included in the value of τ_{c_i} extracted from the atomistic modeling. For the model to meaningfully simulate plate precipitates, two definitions of angle and critical angle are required (Figure 7). The first ($\hat{\phi}$) corresponds to the case when the dislocation is only in contact with one edge of the plate, which is equivalent
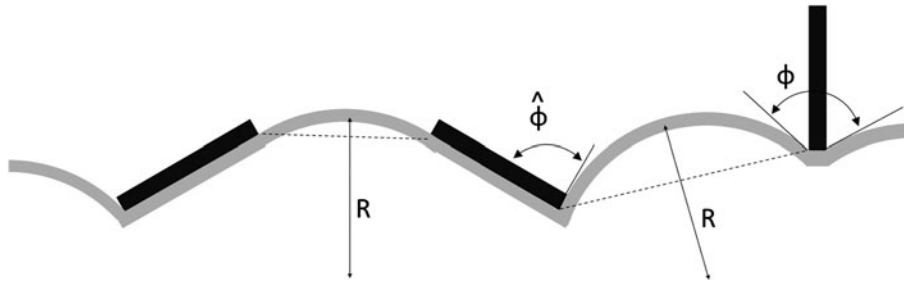
Fig. 7—Schematic illustration of key components of dislocation line tension modeling. Here, a dislocation is pinned by 3 plate precipitates. Between pinning points, it bows out by a radius R. The two measures of angle that dictate precipitate strength in the model are shown.

to the point obstacle case. The second (ϕ) corresponds to the case when the dislocation is interacting with both edges of the precipitate. In both cases, once the bowing angle has reached the critical angle at an edge of the precipitate, the precipitate is considered inactive. The critical bowing angle for a specific interaction is related to ϕ_{c_i} via $\phi_{c_i} = 2\cos^{-1}(\tau_{c_i}\hat{L}_i/Gb)$ and $\hat{\phi}_{c_i} = \cos^{-1}(\tau_{c_i}\hat{L}_i/Gb)$ for the two cases, respectively. $\hat{L}_i$ represents the precipitate spacing in the atomistic simulation cell in which ϕ_{c_i} is measured. An initial validation of the implementation was performed on a system composed of periodic arrays of precipitates consisting of identical interactions, i.e., $\tau_{yp} = \tau_{c_i}$.

The super-Orowan strengths associated with 60 deg dislocation-θ'' precipitate interactions pose a specific challenge as they correspond to $\tau_{c_i}\hat{L}_i/Gb > 1$ leading to imaginary critical angles. To accommodate this, we use an artificially high value of $Gb = 22.6$ N/m in the discrete dislocation simulations. This allows a meaningful critical bowing angle to be defined for the 60 deg dislocation-θ'' precipitate interactions, while only mildly influencing the simulation results (<5 pct error).

Consistent with previous discrete dislocation studies of dislocation-point obstacle interactions,[63] τ_{yp} is found to depend on the simulation cell size. Considering that the propagation of the dislocation line is controlled by the weakest pinning point along its length, τ_{yp} decreases with dislocation length and increases with glide distance (noting that τ_{yp} is the CRSS at which the dislocation traverses the entire simulation cell). In the simulations performed here, the cell sizes are chosen such that the measured value of τ_{yp} is within 5 pct of the value that would be obtained if the simulation cell dimensions matched the grain size, based on our own experience and Nogaret and Rodney.[63]

The simulation cell of the discrete dislocation model was populated with precipitates, both GP zones and θ'' precipitates, following the sizes and densities suggested by the precipitate growth kinetics model that will be described in the next section. The orientation and offset of the precipitates were distributed uniformly in the simulation cell. The precipitates were positioned randomly under the constraint that they neither touch each other nor have centers within $0.3 (w_i + w_j)$, where w_i and w_j are the projected diameters of precipitates i and j, respectively. This approach is qualitatively consistent

with the physics of the precipitation process[66] and simplifies the dislocation dynamics algorithm.

As mentioned at the beginning of this section, the discrete dislocation model is employed to evaluate τ_{yp} at a set of time points during the aging process corresponding to a single set of aging parameters, i.e., Cu concentration and aging temperature. The points are then fit to an aging curve following a standard analytic expression with a single fitting parameter. This approach not only serves to limit the computational expense of the discrete dislocation model (the algorithm has not been optimized) but also, more importantly, provides a simple and effective means to estimate age hardening from the strength contributions of individual components. Specifically, at a given aging time, we consider the total resolved shear strength of a field of precipitates τ_{yp} to be

$$\tau_{yp} = \eta \left[\sum_{i=1}^{N} \left(\tau_{c_i} \frac{\hat{L}_i}{L_i} \right)^{\alpha} \right]^{1/\alpha} \qquad [2]$$

where the index i cycles through all precipitate types and orientations present in the material. $\hat{L}_i$ represents the precipitate spacing used in the atomistic simulation to calculate τ_{c_i}, while L_i represents the spacing between precipitates with characteristics i in the microstructure. η is a fitting parameter that accounts for the collective effect of offset, random precipitate positions, and the interactions between the various precipitates that are not included in the summation. Due to the dense microstructure of precipitates studied here, we choose $\alpha = 2$ consistent with the recent work of.[65]

Once τ_{yp} is obtained for a given distribution of precipitates (whether using the analytic or the discrete dislocation model), the combined strengthening due to both precipitates and solutes can then be written as

$$\tau_y^{\alpha} = \tau_{ys}^{\alpha} + \tau_{yp}^{\alpha} \qquad [3]$$

Consistent with the Dong et al.[65] analysis and the relatively high density of precipitates studied here, we again use $\alpha = 2$ to combine solute strengthening with precipitate strengthening.

The total strength of an Al-Cu alloy results from the dislocation motion being inhibited not only by Cu solute atoms and precipitates but also by grain boundaries, other dislocations, and other crystallographic and

chemical obstacles. The strengthening contribution from these miscellaneous obstacles, $\sigma_{y0} = 20$ MPa, is considered to be constant in this work, i.e., independent of aging time, temperature, and Cu concentration. Thus, we consider the uniaxial yield strength of a polycrystalline Al-Cu alloy as

$$\sigma_y = \sigma_{y0} + T\tau_y \qquad [4]$$

where T is the Taylor factor which for FCC material is $T = 3.06$.[67–69] It is notable that this value of Taylor factor is usually considered as the upper limit and may yield somewhat higher hardness predictions.

In the most heavily referenced experimental studies on Al-Cu age hardening,[17] which we will compare to in this work, strengthening is expressed in terms of Viker's hardness, which is related to uniaxial yield strength by

$$H_v = c_{vp}\sigma_y \qquad [5]$$

where c_{vp} is a constant determined by geometrical factors during experimentation and usually ranges between 2 and 4. Here, we use $c_{vp} = 3.0^*$.

---

*Note that while H_v is usually measured in kgf/mm², σ_y is in MPa. Therefore, one needs to divide the right hand side of Eq. [5] by $g = 9.807$ to get hardness in the units of Vicker's Pyramid Number (VPN).

V. PRECIPITATE KINETICS MODELING

The kinetics of the precipitation process in Al-Cu alloys is complicated by the existence of several precipitate phases, i.e., GP zones, θ'', θ', and θ precipitates, as outlined in the introduction. As a simplification, we ignore the existence of θ' and θ precipitates in this work under the assumption that they only contribute significantly to the overaged material behavior which is not the focus. While ab-initio investigations into the kinetics of Cu precipitation in Al are available in the literature,[70] we were not able to find any existing models that capture the transition from solute to GP zones and θ'' precipitates simultaneously. Thus, we model the precipitation kinetics in this work by piecing together several popular analytic models with the primary goal of simplistically capturing the key phenomena relative to the mechanics modeling.

Following classical theory of phase transformation kinetics,[71,72] the precipitate concentration, $c_p(t)$, at time t relative to the equilibrium concentration of precipitates, c_{pe}, is taken to follow the Johnson, Mehl, and Avrami (JMA) equation,

$$f_p(t) = \frac{c_p(t)}{c_{pe}} = 1 - exp(-k_1 t^n), \qquad [6]$$

where k_1 is the rate constant at the prescribed aging temperature and n is the transformation exponent. The equilibrium precipitate concentration is expressed as $c_{pe} = c - c_{se}$, where c is the total Cu concentration in the alloy and c_{se} is the equilibrium solute concentration at a given temperature. c_{se} is obtained by linearly interpolating the solute equilibrium concentrations of 0.1 wt pct Cu at 373 K (100 °C) and 0.2 wt pct Cu at 473 K (200 °C), as reported in Hornbogen[73] and Massalski.[74] Recent first-principles investigations[70] support the applicability of Eq. [6] for Al-Cu alloys with $n = 1.5$, which is followed here.

Ignoring the overaged precipitates, the JMA equation is also used to describe the concentration of θ'' precipitates, $c_{\theta''}$, relative to the total precipitate concentration

$$f_\theta''(t) = \frac{c_\theta''(t)}{c_p(t)} = 1 - exp(-k_2 t^n) \qquad [7]$$

with k_2 being a second-rate constant related to the rate at which Cu atoms belonging to GP zones become associated with θ'' precipitates. When $k_1 \gg k_2$, k_1 controls the rate of formation of GP zones and k_2 controls the rate of formation of θ'' precipitates. When $k_2 \gg k_1$, GP zones do not form and k_1 controls the rate of formation of θ'' precipitates. The model's ability to capture these key phenomena makes it sufficient for the objectives of this paper.

The total number of GP zones is assumed to be fixed, allowing the GP zone diameter at time t to be expressed as

$$D_{GP}(t) = (D_{GP})_{max} f_{GP}^{1/2}(t) \qquad [8]$$

where $f_{GP}(t) = 1 - f_{\theta''}(t)$ and $(D_{GP})_{max}$ corresponds to the maximum GP zone diameter which we take as 10 nm.[16]

Following experimental observation,[16] θ'' precipitates are assumed to have a constant diameter for $f_p < 0.8$. When $f_p \geq 0.8$, Ostwald ripening of θ'' precipitates is included with their diameter evolving according to the Wagner rule[75]

$$D_{\theta''}^2 - (D_{\theta''})_{min}^2 = k_3(t - t_0) \qquad [9]$$

where $(D_{\theta''})_{min} = 8$ nm and t_0 corresponds to the time at which $f_p = 0.8$. k_3 represents the rate of the ripening process and is considered the third fitting parameter of the kinetics model. With k_3 being a fitting parameter, the exact choice of t_0 is not influential so long as it corresponds to a high f_p value.

For plate precipitates with uniformly distributed offsets, the average distance, L_i, between precipitate centers of a particular type and orientation, i, is[76]

$$L_i = 0.931(0.306\pi D_i h_i / f_i)^{1/2} \qquad [10]$$

where h_i, D_i, and f_i represent the thickness, diameter, and relative concentration of the precipitates with characteristics, i, respectively.

VI. AGE HARDENING PREDICTION OF AL-4 WT PCT CU AGED AT 383 K (110 °C)

Before applying the model to age hardening prediction, the precipitation kinetics rate constants k_1, k_2, and k_3 must be determined. While ideally these values should correspond directly to results from precipitation kinetics experiments, e.g., Yan[77] and Starink et al.,[43] we are not aware of this information for the age hardening

experiments to which we compare our model.[17] Thus, the rate constants k_1, k_2, and k_3 are chosen so that the distinguishing features of the age hardening curve for Al-4 wt pct Cu aged at T_{age} = 383 K (110 °C) match experiments. Specifically, k_1 is chosen so that the GP zone concentration starts saturating at t = 3.5 days; k_2, which controls the transformation from GP zones to θ'' precipitates, is chosen so that the strength plateau ends at t = 20 days; and k_3, which controls the rate of coarsening of θ'' precipitates, is chosen so that the peak hardness occurs at t = 230 days. Accordingly, $k_1 = 2.0 \times 10^{-8}$/s, $k_2 = 1.9 \times 10^{-11}$/s, and $k_3 = 2.4$ 10^{-3} Å^2/s for Al-4 wt pct Cu aged at T_{age} = 383 K (110 °C). The evolution of the concentrations of solute, GP zones, and θ'' precipitates is given in Figure 8(a), and the evolution of the precipitate diameters and effective spacings is giving in Figures 8(b)) and (c), respectively. The relative concentrations of each constituent correspond well with the diffraction observations[17] and are in accordance with traditional understanding. With the kinetics rate constants known, L_i can be computed for the various precipitate types for use in the analytic model and the microstructure can be constructed for the discrete dislocation model as described in Section IV. Two images of representative microstructures used in the line tension simulations are shown in Figure 9. The offsets of the precipitates in the slip plane were uniformly distributed.

Ten discrete dislocation line tension simulations were performed at various aging times for microstructures corresponding to Al-4 wt pct Cu aged at T_{age} = 383 K (110 °C). The minimum size of the dislocation dynamics model was taken as $0.6 \times 0.6 \sim \mu m^2$. The solute hardening contribution is added to the discrete dislocation results, Eq. [2], and the resultant τ_y's are shown in Figure 10. At aging times of 400 days and 1000 days, two realizations were performed to highlight the variation due to the randomness in precipitate microstructure. Fitting the free parameter in the analytic model to the data points generated with the discrete dislocation model, i.e., setting η = 0.64 in Eq. [2], reveals the shape of the well-known Al-Cu aging curve demonstrating both a plateau and peak in strength with aging. For comparison, the analytic model predictions with η = 0.60 and η = 0.70 are also plotted. It is interesting to point out that a constant value of η provides a relatively accurate approximation across the entire range of microstructures that exist during aging. This observation provides justification for our use of the same value of η at different aging temperatures and Cu concentrations.

In addition to enabling quick predictions of age hardening by avoiding discrete dislocation simulations, the analytic model allows the contribution of individual constituents to be assessed. Figure 10 shows that the initial increase in strength with aging is associated with an increase in GP zone strengthening consistent with experiment.[17] The increase in strength as Cu atoms transfer from solute to GP zones is a result of $\frac{\partial \tau_{yGP}}{\partial c_{GP}} > \frac{\partial \tau_{ys}}{\partial c_s}$, where c_{GP} represents the concentration of Cu belonging to GP zones and τ_{yGP} represents the total
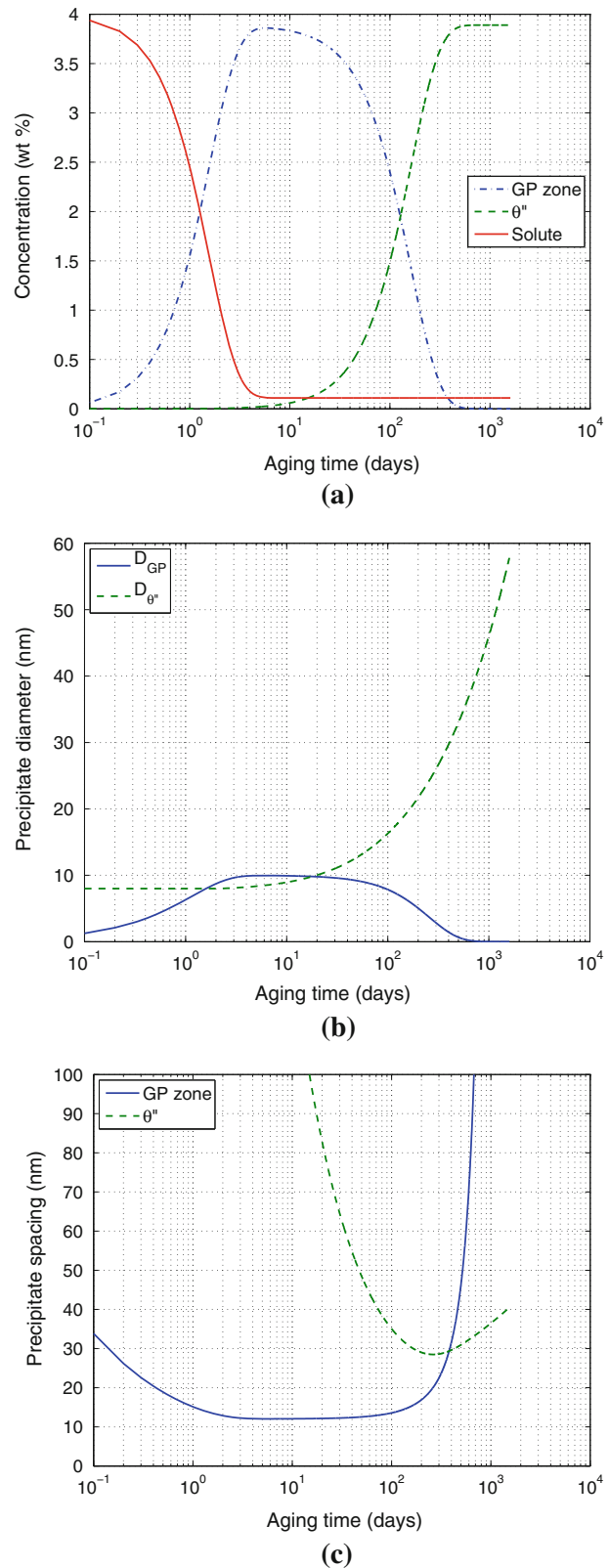

Fig. 8—Precipitation kinetics of age hardening for Al-4 wt pct Cu at T_{age} = 383 K (110 °C): (a) evolution of precipitate and solute concentrations, (b) evolution of average precipitate diameter, and (c) evolution of average center-to-center precipitate spacing.
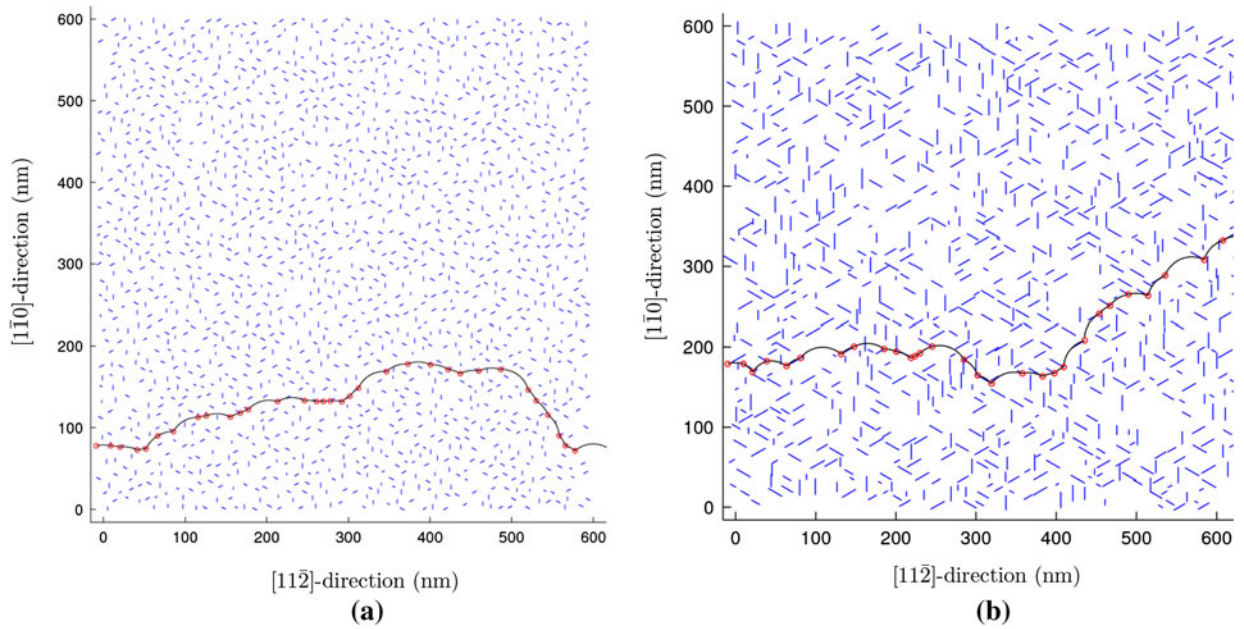
Fig. 9—Snapshots of dislocation line tension model for Al-4 wt pct Cu alloy aged at T_{age} = 383 K (110 °C): (a) underaged, 1 day, (b) at optimum hardness, 230 days. The blue line segments represent sections of precipitates which intersect the slip plane. The black line represents the dislocation and the red circles represent its contact points with the precipitates.
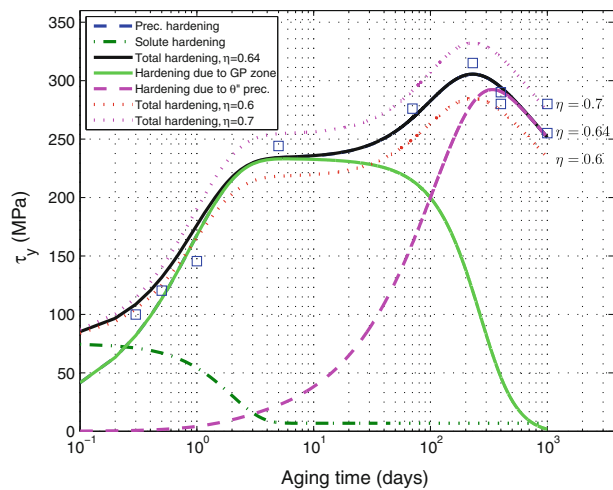

Fig. 10—0 K resolved shear strength *vs* aging time predictions for Al-4 wt pct Cu aged at T_{age} = 383 K (110 °C). The data points were obtained using the dislocation line tension simulations and the curves represent the fitted simplified continuum model described in the text. The solute and precipitate hardening curves correspond to η = 0.64 in the simplified continuum model.

strengthening due to GP zones. The inequality (see Appendix D) shows that strength will increase as Cu atoms transfer from solute to GP zones until $c_{GP} > 0.66 c_s^{7/12}$, at which point further transfer produces a decrease in strength (for the Al-4 wt pct Cu alloy aged at 383 K (110 °C)).

The second increase in strength, beginning at ~30 days of aging time, is due to both an increase in the concentration and size of θ'' precipitates, consistent with experiment.[17] In general, the GP zone to θ''

precipitate transformation would be expected to bring a strength increase when $\tau_{c_{\theta''}} > \tau_{c_{GP_i}} \sqrt{2 D_{\theta''} / D_{GP}}$, considering Eqs. [B1] and [10], where $\tau_{c_{GP_i}}$ and $\tau_{c_{\theta''_i}}$ represent values of τ_{c_i} from the atomistic simulations detailed in Section II with a consistent simulation cell size. While the diameters of the two precipitate types evolve during the transformation, at its peak, ~9 nm GP zones transform to ~15 nm θ'' precipitates. This sufficiently satisfies the inequality given above.

The increasing size of the θ'' precipitates is governed by the coarsening law, Eq. [8]. As the precipitates coarsen, they individually provide greater resistance to dislocation glide (Figures 3, 5); however, the individual strengthening is counteracted by an increase in precipitate spacing (Eq. [10]) which reduces their collective effect (Figure 2). In general, for plate precipitates, coarsening leads to strengthening when $\frac{\partial \ln \tau_c}{\partial \ln D} > \frac{1}{2}$. Here, the results of Figure 5 combined with Eq. [2] predict that coarsening will strengthen when $D_{\theta''_i} < 15$ nm. Thus, the strengthening observed in Figure 10 after 100 days of aging can be solely attributed to the transformation of Cu from GP zones to θ'' precipitates, as coarsening is detrimental to strength when $D_{\theta''_i} > 15$ nm.

After a majority of precipitates have transformed into θ'' precipitates at ~300 days, the strength of Al-4 wt pct Cu decreases with time as coarsening is the only active precipitate evolution mechanism. At ~1000 days of aging at 383 K (110 °C), θ'' precipitates would grow to the size where θ' precipitate formation would be expected. Considering the dislocation interaction mechanisms observed for θ'' precipitates, it is reasonable to assume that θ' precipitates would have similar strengths. Thus, we hypothesize that the formation of θ' precipitates (not considered in the model) in the later stages of

aging would expedite the rate of softening relative to the current model.

VII. EFFECT OF Cu CONCENTRATION AND AGING TEMPERATURE

The aging temperature and the Cu concentration are two key parameters that are often adjusted to tailor alloy performance. Both affect strength *via* precipitation kinetics and equilibrium concentrations. In this section, these effects are examined within the modeling framework developed in the previous sections. First, the effects of Cu concentration are discussed, then aging temperature. The rate, k_1, at which Cu atoms transform from solute to GP zones in a solutionized and then quenched Al-Cu alloy is a complex function of the Cu concentration. k_1 depends on the homogeneous nucleation rate of GP zones and the GP zone growth rate. The factors affecting k_1 are discussed in[43,72,78] with a first-order estimate derived as

$$k_1 = k_{1_0}(c - c_{se})^{2.5} \exp\left(-\frac{E_{eff}}{k_B T_{age}}\right) \quad [11]$$

where k_{10} is a constant, c is the initial concentration of Cu in solute in the quenched alloy, c_{se} is the equilibrium solute concentration, k_B is the Boltzmann constant, and E_{eff} is an effective activation energy barrier for the process, which is a function of the activation energy barrier for diffusion and the activation energy barrier for GP zone nucleation. Here, we assume that k_2 takes a similar form to k_1. The rate constant for coarsening, k_3, is expected to take a different form. Following Wagner[75] (see page 21 of[79]),

$$k_3 = \frac{64 K V_a}{81 k_B T_{age}} c_{se}, \quad [12]$$

where V_a is the atomic volume of Cu. The constant K includes the diffusion coefficient of Cu in bulk Al and the precipitate-matrix interface energy density. It can be written in the form $K = K_0 \exp\left(-\frac{E_{eff}^w}{k_B T_{age}}\right)$ with K_0 being a constant and E_{eff}^w being the corresponding effective activation energy barrier.

Figure 11 depicts the age hardening curves from the model with $\eta = 0.64$. The variation of the curves with Cu content (2.5 to 4.5 wt pct) displays the same qualitative features as observed in experiment.[17] The aging time to the first strength plateau and the time to the peak hardness increase with decreasing Cu content. The strength level along the entire aging curve and the values associated with the plateau and the peak decrease with decreasing Cu content. Quantitatively, the change in strength with concentration is reasonably consistent with the experiment. However, at short aging times (~ a few hours), the ratio between the 2.5 and 4.5 wt pct strengths is considerably different than the experiment. While this difference could be due to not considering thermally activated plasticity in the model, it might also be indicative of a varying value of σ_{y0} with solute
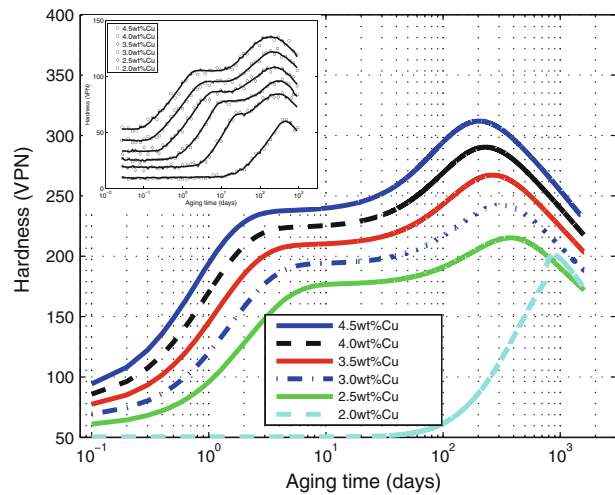

Fig. 11—0 K (−273 °C) hardness *vs* aging time predictions for Al-Cu aged at T_{age} = 383 K (110 °C) with various Cu concentrations. Inset shows experimental data at 300 K from Ref.[17]

concentration and inaccuracies in the solute hardening model.

A more pronounced disagreement between the model predictions shown in Figure 11 and the experimental data[17] is associated with the width of the strength plateau, *i.e.*, the duration of aging time for which the strength is approximately constant. The experimental data display a decreasing strength plateau width with decreasing Cu concentration on the standard semi-log aging plot. The decrease in the strength plateau width is driven by slower GP zone precipitation at decreased Cu concentrations (noting that the aging time to the end of the strength plateau is governed by θ'' precipitate formation which is more mildly affected by Cu concentration both in our model, Figure 11, and experiments[17]). At concentrations below 2.5 wt pct Cu, a strength plateau no longer exists in the experiments. This occurrence is in accordance with the GP zone solvus concentration at 383 K (110 °C).[74] The linear scaling of the GP zone formation rate kinetics model used here does not predict the rate going to zero as the solvus concentration is approached. This represents a shortcoming of the current kinetics modeling formulation. In future work, it would make sense to formulate the kinetics in a manner that is consistent with the thermodynamic stability of the precipitate phases. One way to avoid this heuristic approach would be to perform a first-principles-based prediction of the formation of the precipitate phases at given temperature and solute concentration, similar to the study reported by Wang *et al.*,[70] which is out of the scope of the present work. With the current model, the creation of a qualitatively accurate aging curve at concentrations below 2.5 wt pct Cu can only be created by explicitly prohibiting GP zone formation, as was done in Figure 11.

The effect of aging temperature on the age hardening curve has also been examined by modeling the aging process at 403 K (130 °C) and 438 K (165 °C) (Figure 12). The temperature scaling of the kinetics rate constants
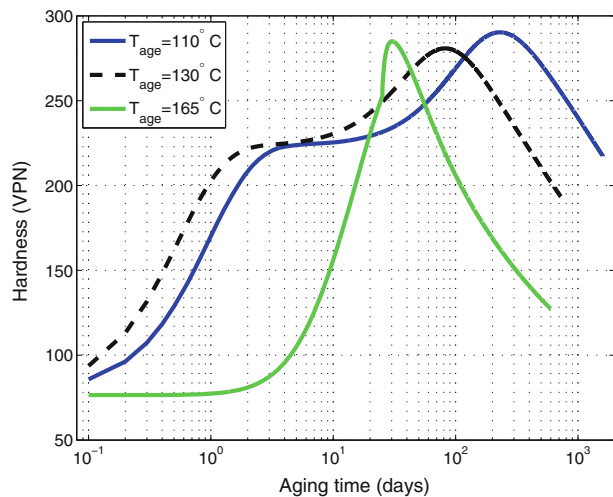
Fig. 12—0 K hardness *vs* aging time predictions for Al-4 wt pct Cu aged at different temperatures.

associated with GP zone nucleation and growth, θ'' precipitate nucleation and growth, and θ'' coarsening was obtained from Eqs. [11] and [12] with estimated values of the effective activation energies. As a whole, the aging process in Al-Cu alloys is typically associated with an activation energy ranging from 0.78 to 1.35 eV *via* differential scanning calorimetry (DSC) experiments.[43,80,81] However, more recent DSC work by Bassani *et al.*[82] has been able to specifically associate calorimetric data with GP zone and θ'' formation. Here, we will use their values of 0.57 eV for GP zone formation and 0.86 eV for θ'' precipitate formation. In the absence of data, we use 0.86 eV for coarsening as well.

For the 4 wt pct Cu alloy, increasing the aging temperature from 383 K (110 °C) to 403 K (130 °C) accelerates the aging process by accelerating the formation, growth, and coarsening of precipitates as seen in Figure 12. The acceleration of the entire aging curve over this temperature range is consistent with experimental observations.[17] In the range of parameters investigated here, the peak strength is a function of the correspondence between the θ'' precipitate formation rate and the coarsening rate, as well as the amount of Cu available for precipitation. All three are affected by aging temperature. Nonetheless, only slight changes in the peak strength are observed in the model between 383 K (110 °C) and 403 K (130 °C) aging temperatures, consistent with experimental observations.

For 4 wt pct Cu, the GP zone solvus temperature is approximately $T_{solvus} = 423$ K (150 °C).[74] Therefore, aging above 423 K (150 °C) will not produce GP zones, leading to aging curves that do not display strength plateaus.[17] The current model as formulated does not capture this feature as the kinetics modeling predicts GP zone formation at all realistic aging temperatures. In future efforts, this inconsistency could be addressed using a kinetics modeling that accounts for the thermodynamic stability of precipitate phases, as performed in[70] using first-principles calculations.

Noting this deficiency in the model, we produced an aging curve at 438 K (165 °C) (Figure 12) by explicitly

prohibiting the growth of GP zones. The qualitative features of the curve agree with experiment,[17] with the exception of the kink that exists at 14 days of aging time. The kink results from the sudden start of coarsening kinetics in our model when 80 pct of the Cu atoms has transformed from solute to precipitates. Obviously, the abrupt start of coarsening in the model is unrealistic. Further, the model predicts the formation of unrealistically large θ'' precipitates, (diameters larger than 100 nm). In reality these large θ'' precipitates would transform into tetragonal θ' precipitates.[17] Experimental observations suggest that optimum hardness occurs for 4 wt pct Cu aged at 438 K (165 °C) during the transition from θ'' to θ' precipitate formation.[17]

VIII. ROLE OF THERMAL ACTIVATION AND DIRECT COMPARISON TO EXPERIMENT

The age hardening predictions presented in the previous sections significantly overpredicted alloy hardness because they ignored the role of thermal activation in dislocation-precipitate and dislocation-solute interactions. Specifically, the predictions were formulated directly from atomistic simulations of dislocation-precipitate interactions conducted at zero temperature and an analytic solute hardening model that did not include temperature and strain rate effects. The aim of this section is to interpret the athermal predictions relative to typical experimental conditions, *i.e.*, $T \approx 300$ °K and $\dot{\gamma} \approx 10^{-3}$/s.[28]

While thermal activation is thought to play a significant role in dislocation-solute interactions, its significance in dislocation-precipitate interactions is unclear. A collection of experiments suggests that precipitate strengthening is relatively independent of thermal activation,[23,26,83] while others show evidence to the contrary.[28,84] We note that the study by[28] is of particular significance in that it examined underaged Al-Cu alloys with large populations of GP zones and θ'' precipitates. Atomistic simulations have not necessarily clarified the issue. Bacon and coworkers' simulations[33,40] suggest that precipitate strengths are significantly affected by thermal activation with 300 K strengths differing by a factor of 1.5 to 2.0 compared to 0 K, while[85] report that dislocation-nanovoid interactions are largely temperature independent (noting that there are many similarities between dislocation-void and dislocation-precipitate interactions).

Here, thermal activation is investigated using the same underlying framework and assumptions for both solute and precipitation hardening. The applied load τ is related to plastic strain rate $\dot{\gamma}$ in the presence of thermal activation[54,84] by

$$\frac{\tau}{\tau_{inst}} = 1 - \left(\frac{k_B T}{\Delta E_0} \ln \frac{\dot{\gamma}_0}{\dot{\gamma}} \right)^{2/3}. \qquad [13]$$

where τ_{inst} is the load at which the thermally activated events occur instantaneously and ΔE_0 is the activation energy barrier. For the sake of completeness, the above
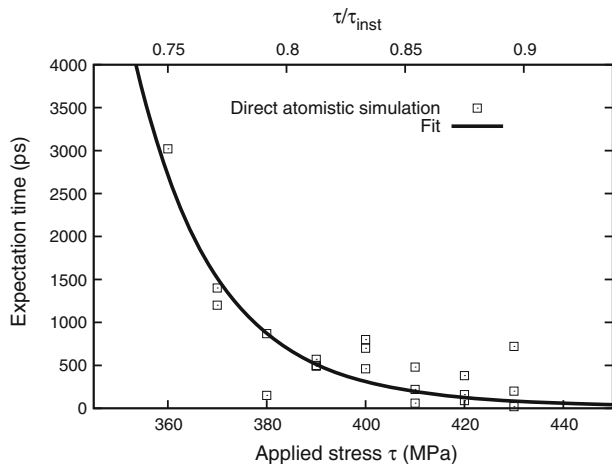
Fig. 13—Expectation time for an edge dislocation to overcome a 4.4 nm GP zone (60 deg interaction and L = 7.94 nm) as a function of fixed applied shear stress at 300 K. The instantaneous applied shear stress, τ_{inst}, is 460 MPa. The fit corresponds to Eq. [E2].
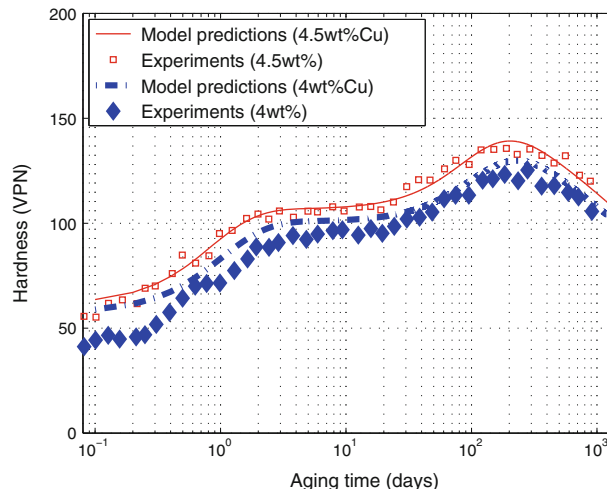

Fig. 14—300 K hardness *vs* aging time predictions for Al-Cu aged at T_{age} = 383 K (110 °C). Experimental data are from Silcock *et al.*[17]

relation is derived in Appendix E. For solute hardening, the energy barrier, ΔE_0, follows directly from Eq. [C6] of the semi-analytic solute hardening model. Thus, the only unknown parameter is $\dot{\gamma}_0$, which represents the plastic strain rate that would occur if the controlling thermally activated events were to happen instantaneously. Here, we take $\dot{\gamma}_0 = 10^4$ consistent with Leyson *et al.*,[54] noting that this is a physically reasonable value, considering the mobile dislocation density in Al-Cu alloys, $\rho_m \approx 10^{10}$/ m^2[86]; the velocity of a free dislocation in Al at the yield stress $v \approx 1$ nm/ps,[87] and the relation $\dot{\gamma} = \rho_m b v$.[88] Using T = 300 K, ΔE_0 = 2.78 eV, $\dot{\gamma} = 10^{-3}$/s, and $\dot{\gamma}_0 = 10^4$/s, a thermal activation correction factor of τ/τ_{inst} = 0.72 is obtained for solute hardening.

For precipitate hardening, the unloaded energy barrier is not readily extractable from the 0 K simulations preformed in Section II. It must either be measured directly using a chain of states method[89] or inferred from a set of direct molecular dynamics simulations.[90,91] In this work, we have taken the latter approach. The investigation focused specifically on a 60 deg interaction between an edge dislocation and a 4.4 nm diameter GP zone, as studied in Section II–A. The molecular dynamics simulation cell size in the Z directions was $L \approx 7.8$ nm. At each fixed load, multiple molecular dynamics simulations were performed at T = 300 K with different initial random velocity seeds. The simulation time before the dislocation overcame the GP zone is shown in Figure 13. At a fixed load, the mean time, $\bar{t}$, for the dislocation to overcome the GP zone is the inverse of the rate, $\tilde{v}$, associated with the thermally activated event. Accordingly, the data in Figure 13 can be described by Eqs. [E1] and [E2]. The best fit is obtained with $\Delta E_0 = 0.98$ eV and $\tilde{v}_0 = 1/\bar{t}_0 = 4.25 \times 10^{10}$/s. With ΔE_0 in hand, Eq. [13] can be used to predict a thermal activation correction factor for a specific temperature and strain rate as was done for solute hardening. Using T = 300 K, $\Delta E_0 = 0.98$ eV, $\dot{\gamma} = 10^{-3}$/s, and $\dot{\gamma}_0 = 10^4$/s, a factor of

τ/τ_{inst} = 0.44 was obtained. Interestingly, this suggests that thermal activation plays a more significant role in this dislocation-GP zone interaction than in solute hardening.

The thermal activation correction factor computed above is assumed to apply to all dislocation-precipitate interactions considered in the age hardening model. This assumption was required in light of our finite computational and human resources and is not necessarily consistent with previous experimental[28] and atomistic simulation[39] results which indicate that the role of thermal activation is highly specific to the particular features of individual dislocation-precipitate interactions. An additional assumption implicit to the generation of finite temperature aging curves is that the effect of thermal activation on individual dislocation-precipitate interactions is proportional to the effect of thermal activation on an entire glide plane with a collection of dislocations and precipitates. We point the interested reader to Xu and Picu[64] for further discussion of this point.

Utilizing the thermal activation correction factor for both solute and precipitate hardening, age hardening predictions for both 4 and 4.5 wt pct Cu aged at T_{age} = 383 K (110 °C) and deformed at T = 300 K (27 °C) with a strain rate of 10^{-3}/s have been produced. The curves are directly compared to the experimental data from[17] in Figure 14. Overall, the model predictions are found to agree very well with experiments considering the number and complexity of ingredients involved in the model and the lack of mechanics fitting parameters. The agreement of the strength plateau and peak strength is particularly noteworthy in light of the significant assumptions noted in the previous paragraph. The most significant discrepancy between the model predictions and the experimental curves involves the effect of Cu concentration on strength at the earliest aging times. As with the athermal predictions in Section III, the solute hardening model underpredicts this effect.

IX. SUMMARY AND CONCLUSIONS

Significant improvements in computational power and methodologies[54,92] in the last decade have led to unparalleled advancements in the quest to quantitatively connect mechanical behavior to underlying atomic-scale processes. Nonetheless, a direct prediction of age hardness solely from atomistic principles has remained a formidable challenge. As a step toward this goal, the work presented here strives to connect atomic-scale strengthening mechanisms to the age hardening behavior of Al-Cu alloys using a hierarchical multiscale approach. Other than the fitting of the interatomic potential to experimental and electronic structure simulation data, which was done externally to this work by other authors, the mechanical modeling did not involve any free parameters. To capture the complex microstructural evolution of an Al-Cu alloy (Cu solute $\rightarrow$ GP zones $\rightarrow$ θ'' precipitates), simple kinetics models from the literature were utilized. The kinetics modeling involved three fitting parameters which governed the rate at which the precipitates formed, grew, and coarsened. The fitting parameters were chosen so that key features of the aging curve aligned in time with experimental data for 4 wt pct Cu aged at 383 K (110 °C). Overall, the strength values of the predicted aging curve corresponded remarkably well with experimental data. Considering the scale of the model and lack of mechanical fitting parameters, its general agreement with experiment is remarkable. With that said, the primary value of this effort is not that the model reproduced experimental data, but what was learned in the quest to do so.

At the lowest scale of the model, the atomistic simulations of dislocation–GP zone and dislocation–θ'' precipitate interactions revealed significant complexity beyond textbook understanding. Full dislocation looping, full dislocation cutting, and leading partial cutting with trailing partial looping were observed depending upon the details of the interaction. Contrary to traditional wisdom, dislocation looping occurred in some interactions involving very small precipitates. However, the lack of thermal activation and the validity of the interatomic potential motivate caution when connecting this observation to a real Al-Cu alloy deformed at room temperature. Precipitate cutting occurred by an unzipping mechanism, which is not considered in many traditional models for precipitate strengthening. On the whole, the variety and complexity of the dislocation-precipitate interactions complicate continuum precipitate strengthening predictions and motivate atomistic analysis.

Precipitate strengthening was found to scale quite well with the simple $1/L$ relation even when L was comparable to the precipitate diameter. This suggested that more sophisticated relations between L, D, and strength may not always be warranted. In general, precipitate strength was found to be higher for 60 deg dislocation-precipitate interactions than for 0 deg interactions. The maximum strength of dislocation-GP zone interactions was found to be 0.35 and 0.55 of the theoretic Orowan strength depending upon the orientation of the interaction. The maximum strength of dislocation-θ'' precipitate interactions was found to be 0.50 and 1.75 of the Orowan strength depending upon the orientation of the interaction. The super-Orowan strengths of the dislocation-θ'' precipitate interactions result from the cross-slip of the bowed-out dislocation segments. Based on observations of cross-slip strengthening in screw dislocation-precipitate interactions in our previous work,[39] we are uncertain of the existence of this mechanism and the subsequent super-Orowan strengths under ordinary experimental conditions. In this regard, it is important to note that it is the cross-slip strengthening that makes larger (<15 nm) θ'' precipitates significantly stronger than GP zones and thus leads to the peak in the age hardening curve. If the Orowan strength is taken as the maximum dislocation-precipitate interaction strength in the model, the strength increase due to the transition from GP zones to θ'' precipitates would be small. This would produce an aging curve qualitatively different from that observed in the experiment, without the plateau-then-peak shape. Based on our experience, two further studies would go a long way toward illuminating this matter. First, a thorough analysis of the role of thermal activation is needed for the dislocation-θ'' precipitate interactions with super-Orowan strengths. Second, both screw and edge dislocations must be considered.

Our first attempt to model solute hardening involved directly simulating the motion of a dislocation through a field of solute atoms. The simulations resulted in an unrealistically high athermal strength. This result was attributed to a very high Al-Cu bond strength. So that this outcome did not derail our effort, we then attempted to predict solute hardening via a newly developed semi-analytic solute hardening model that uses atomistically computed Cu solute–edge dislocation interaction energies as input. While these predictions were still significantly larger than the corresponding DFT values in the literature,[54] they were usable in the age hardening model. Broadly, the solute hardening section highlights the importance of both matrix-solute bond strengths and dilute heat of solution energies in interatomic potentials when solute hardening predictions are desired.

While the formulation of the solute hardening model directly provides the shear strength for a dislocation to propagate through a field of solute atoms, the shear stress required for a dislocation to propagate through a field of precipitates requires additional consideration beyond the atomistic studies of a dislocation interacting with an equally spaced periodic array of identical precipitates. Although a considerable amount of work exists on this topic, the majority of the work has focused on point precipitates rather than plates. This motivated the construction of a continuum dislocation line model. A particular challenge in employing the model involved the incorporation of the super-Orowan strengths of the dislocation θ'' precipitate interactions. This was overcome using an artificially high value of $G\,b$ in the model. Parametric studies suggest that this induced an error of less than 5 pct in the predictions. In addition to the

continuum dislocation line model providing a means for connecting the atomistic simulations of dislocation-precipitate interactions with macroscopic strengths, it illuminated the utility of simple analytic approaches at doing the same. Specifically, we found that a quadratic law addition of individual precipitate mean strengths weighted by a knockdown factor can describe the strength to propagate an edge dislocation on a slip plane populated by a set of randomly positioned plate precipitates with different offsets and strengths. A factor of 0.64 was found to work reasonably well for the span of the Al-Cu aging curve examined here.

To quantitatively compare the model to experiments, thermally activated plasticity must be considered. This task is straightforward with the semi-analytic solute hardening model as it directly provides the energy barrier associated with dislocation motion through a field of solutes. However, for dislocation-precipitate interactions, additional atomistic simulations are required at finite temperature. Focusing on a specific edge dislocation-GP zone interaction, we found that thermal activation can play a large role in this interaction with the strength under typical experimental conditions, *i.e.*, 300 K and $\dot{\gamma} = 10^{-3}$/s, being 44 pct of the athermal strength. The generality of this result to other dislocation-precipitate interactions is unclear, providing motivation for further investigation.

Considering the development of the model in total and the comparison of its predictions to experimental age hardening curves, two substantial outstanding issues exist. First, the initial alloy strengths predicted by the model (due primarily to solute hardening) do not scale as strongly with Cu concentration as experimental data. Second, the plateau-then-peak behavior of the predicted aging curve is the result of a cross-slip strengthening mechanism that may not occur under ordinary experimental conditions. Specifically, for the plateau-then-peak to exist in the aging curve, the θ'' precipitate strength must be significantly greater than the GP zone strength. One way for the plateau-then-peak behavior to exist, without the cross-slip super-Orowan strengthening mechanism of θ'' precipitate interactions, would be for the actual GP zone strengths to be lower than what our atomistic simulations predict. This is plausible considering that the Al-Cu interactions are likely overpredicted with the interatomic potential that we have used here, as indicated from the solute hardening model. Thus, GP cutting may be more prevalent than predicted, making GP zone strengths significantly lower than the Orowan strength of θ'' precipitates.

In general, this work highlights that mechanism-based plasticity modeling is still faced with considerable challenges of both breadth and depth. The complexity of dislocation-precipitate interactions call for many more simulations to be performed before the interactions can be fully characterized. More broadly, the characterization of the vast space of dislocation-grain boundary interactions will likely prove even more challenging. At the same time, more accurate (and most likely computationally demanding) interatomic interaction models are needed to obtain results that better connect to relevant engineering alloys. Furthermore, the effects of thermal activation must be considered, something which often requires a considerable amount of additional computational cost and analysis beyond what is required for athermal simulations. With that said, computational methods and resources continue to improve, making the above challenges appear evermore surmountable in the future.

APPENDIX A: ATOMISTIC MODELING OF PRECIPITATION HARDENING

The atomistic simulations were carried out using the freely available open source LAMMPS code.[93] The code was modified to use a recently developed Al-Cu empirical potential developed by Apostol and Mishin.[57] The potential is an angular-dependent extension of the embedded atom method (EAM)[94,95] where the potential energy of the system is

$$E_{tot} = \frac{1}{2}\sum_{i,j(j\neq i)}\Phi_{ij}(r_{ij}) + \sum_i F_i(\bar{\rho}_i) + \frac{1}{2}\sum_{i,\alpha}(\mu_i^\alpha)^2$$
$$+ \frac{1}{2}\sum_{i,\alpha,\beta}(\lambda_i^{\alpha\beta})^2 - \frac{1}{6}\sum_i \nu_i^2. \quad [A1]$$

Indices i and j enumerate atoms and the superscripts α, β = 1, 2, 3 refer to the Cartesian directions. The first two terms, taken together, represent regular EAM contributions, where Φ_{ij} is the pair-interaction potential and F_i is the embedding energy of atom i with $\bar{\rho}_i$ loosely representing the electron density. The three remaining terms represent the angular dependence through dipole and quadrupole distortions. The details of the potential can be found in Apostol and Mishin[57] and Mishin *et al.*[95] We validated our implementation by comparing relaxed cohesive energies, vacancy formation energies, surfaces energies, heats of solution, and formation energy for the θ'' (Al$_2$Cu) phase with independent values provided by Apostol and Mishin.[57] The simulation cell (Figure A1) consisted of an FCC Al lattice, bounded by $(\bar{1}10)$, (111), and $(11\bar{2})$ faces in X, Y, and Z directions, respectively. Periodic boundary conditions were applied in the X and Z directions, and the Y surfaces were used to apply the load. Starting from a perfect lattice, a precipitate was created by simply changing selected atom types to Cu. The continuum displacement field of an edge dislocation was used to create a dislocation in the center of the simulation cell ($X = Y = 0$) with a line direction parallel to the Z axis and the burgers vector $\vec{b} = 1/2[\bar{1}10]$.

Because GP zones and θ'' precipitates only form on {100}-type planes, there are only three physically relevant orientations by which they interact with edge dislocations, two of which are crystallographically
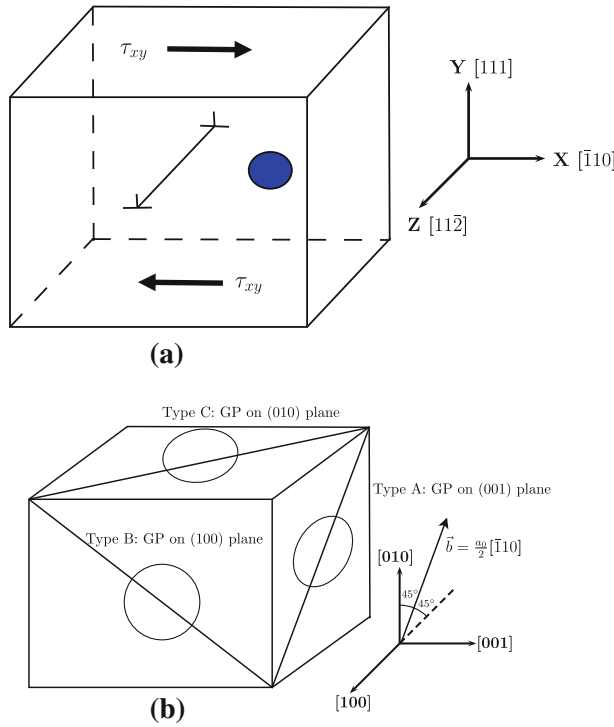
Fig. A1—(*a*) Simulation cell with an edge dislocation and GP zone, (*b*) 3 possible GP zone orientations with respect to the Burgers vector of the dislocation. Type A is referred to as a 0 deg interaction while types B and C are considered equivalent and refered to as 60 deg interactions.

equivalent. The Burgers vector of the edge dislocation will either be at an angle of 60 deg from the precipitate plane or be parallel to it (Figure 1). Thus, we will refer to dislocation–precipitate interactions as either being 60 or being 0 deg in nature. As a simplification, we assume that GP zones are monolayers of Cu atoms with a 100 pct Cu content, while θ'' precipitates are two Cu layers separated by three Al layers.[14,16]

The minimum cell size was approximately $34 \times 42 \times 16$ nm^3 and contained approximately 1.4 million atoms. For the simulations with large GP zones and θ'' precipitates, a larger cell size was used (with largest cell size being approximately $68 \times 44 \times 64$ nm^3 consisting of 11 million atoms). In all cases, box size studies were performed to verify that simulation cell boundary forces were negligible in the X and Y directions. The effect of cell size in the Z direction will be discussed later; however, we note that the cell sizes in the Z direction that we explored are consistent with experimental observations of GP zone and θ'' spacing.[17,28]

Prior to loading, NPT dynamics were performed for 50 ps to relax the system and alleviate out-of-balance forces and net stresses. The system was then loaded in shear by subjecting the atoms near the top and bottom Y surfaces to a constant traction in the X direction given by

$$f_{\text{top}} = \frac{\tau_{xy}A_{xz}}{N}, \qquad f_{\text{bottom}} = -\frac{\tau_{xy}A_{xz}}{N} \qquad [\text{A2}]$$

for top and bottom Y surfaces, respectively, where τ_{xy} is applied shear stress, A_{xz} is the surface area, and N is the number of atoms on the respective surfaces. The applied shear stress was increased quasi-statically until the dislocation breaks free from the precipitate. At each load step of 5 MPa, non-linear conjugate gradient was performed to minimize the out-of-balance forces to less than 10^{-8} eV/Å.

APPENDIX B: ANALYTIC RELATIONS FOR CRITICAL RESOLVED SHEAR STRENGTH OF THE PRECIPITATE, τ_C

Assuming a fixed dislocation line tension, ϕ_c is an intrinsic measure of the strength of the precipitate. Using a simple line tension model and ignoring dislocation self-interactions, the critical stress required for a dislocation to shear a precipitate can be written as

$$\tau_c = \frac{2T}{bL}\cos(\phi_c/2) \qquad [\text{B1}]$$

with T being the line tension of the dislocation. Note that this relation suggests τ_c scales as $1/L$.

In the limit of an impenetrable precipitate, the dislocation will bow into a configuration with neighboring segments on each side of the precipitate perpendicular to the dislocations' original glide direction, *i.e.*, $\phi_c = 0$. In this situation, the dislocation segments will collapse *via* the Orowan looping mechanism,[49] with a critical stress of

$$\tau_c^{\text{Orowan}} = \frac{2T}{bL} \qquad [\text{B2}]$$

From continuum elasticity theory, $T \approx Gb^2/2$, where G is the shear modulus of the matrix material. This leads to $\tau_c^{\text{Orowan}} = \frac{Gb}{L}$ and $\tau_c = \frac{Gb}{L}\cos(\phi_c/2) = \tau_c^{\text{Orowan}}\cos(\phi_c/2)$ for Orowan looping and shearing, respectively. A simple modification is often used to extend these relations into a domain where D is not negligible with respect to L.[26]

$$\tau_c^{\text{BH}} = \frac{Gb}{L - D_p}\cos(\phi_c/2), \qquad [\text{B3}]$$

with $L - D_p$ representing the distance which is available between neighboring precipitate edges for the dislocation to bow-out and D_p being the projected cross-sectional diameter of the precipitate along the dislocation line. Because the above expressions ignore dislocation self-interactions, they overestimate precipitate strengthening. Specifically, the attraction between the two segments of dislocation on each side of the precipitate will promote a more acute bowing angle as well as Orowan looping before $\phi_c = 0$ deg. A semi-empirical expression incorporating self-interaction effects has been given by Scattergood and Bacon[50] by fitting to numerical results,

$$\tau_c^{\text{SB}} = \frac{Gb}{2\pi AL}\left[ln(D^{-1} + L^{-1})^{-1} + B \right] \qquad [\text{B4}]$$

where B is a fitting parameter and $A = 1$ when the dislocation is initially pure edge and $(1 - v)$ when pure screw with v being the Poisson's ratio.

APPENDIX C: DERIVATION OF SOLUTE HARDENING

The model is built upon an interaction energy function between a solute atom and a dislocation, $U(x_i, y_j)$, with x_i and y_j describing the position of the lattice site of the solute atom with respect to a dislocation with a line direction along the z-axis. Using $U(x_i, y_j)$, which is computed from atomistic simulation, the change in energy associated with the movement of a straight dislocation in a field of random solutes a distance w in the direction x can be written as

$$\Delta \hat{E}_p(w) = \sum_{ij} n_{ij}\big(U(x_i - w, y_j) - U(x_i, y_j)\big) \quad [C1]$$

where n_{ij} is an independent random variable representing the number of solute atoms at position (x_i, y_j) along the dislocation line. Considering that the solute locations are uncorrelated, the typical change in energy associated with the movement of a straight segment of dislocation of length, ξ, can be written using a correlation function

$$\chi(w, y_j) = \sum_i U(x_i - w, y_j)U(x_i, y_j) / \sum_i U^2(x_i, y_j), \quad [C2]$$

as

$$\Delta E_p(\xi, w) = -\sqrt{\frac{c_s \xi}{\sqrt{3}b}\left[2\sum_{i,j}\{1 - \chi(w, y_j)\}U^2(x_i, y_j)\right]} \quad [C3]$$

with c_s being the solute concentration. For a finite w, only a finite region near the dislocation segment needs to be considered to compute ΔE_p.

The heterogeneity of the energy landscape experienced by the dislocation promotes a curved dislocation line. In the model, the curvature of the dislocation line is approximated as a series of straight dislocation segments of length ξ that exist at discrete increments of w in the glide direction. The extra line energy due to a segment of dislocation length ξ gliding a distance w away from its neighboring segments can be written as

$$\Delta E_{el}(\xi, w) = \Gamma \frac{w^2 L}{4\xi^2} \quad [C4]$$

with Γ representing the line energy.

The total energy change associated with the glide of a segment of dislocation from an originally straight dislocation is the sum of its change in line energy and change in interaction energy.

$$\Delta E_{tot}(\xi, w) = \Delta E_{el} + \frac{\Delta E_p L}{2\xi} \quad [C5]$$

By minimizing this equation in terms of ξ and w, characteristic length scales ξ_c and w_c can be obtained.

Considering that the strength-controlling energy barriers to dislocation glide result from segments of dislocation length ξ_c that must move from a typical favorable interaction energy fluctuation past a typical unfavorable interaction energy fluctuation over a distance of w_c while regaining the line energy $\Delta E_{el}(\xi_c, w_c)$, the typical energy barrier to the glide of a dislocation segment is

$$\Delta E_b(\xi_c, w_c) = \sqrt{2}\Delta E_p(\xi_c, w_c) - \Delta E_{el}(\xi_c, w_c) \quad [C6]$$

Finally, assuming a sinusoidal energy profile with a peak of ΔE_b over a distance of w_c provides the zero-temperature shear stress needed to move a typical segment of dislocation forward,

$$\tau_{ys} = \frac{\pi}{2}\frac{\Delta E_b}{b\xi_c w_c} \quad [C7]$$

APPENDIX D: HARDENING CONTRIBUTIONS

The strength of the Al-Cu alloy will increase as Cu atoms transfer from solute to GP zones if $\frac{\partial \tau_{yGP}}{\partial c_{GP}} > \frac{\partial \tau_{ys}}{\partial c_s}$ with $c = c_{GP} + c_s$ where c_{GP} represents the concentration of Cu belonging to GP zones and τ_{yGP} represents the strengthening due to GP zones. While $\frac{\partial \tau_{ys}}{\partial c_s}$ can be explicitly expressed in terms of c_s, i.e., $\tau_{ys} \propto c_s^{2/3}$ (Section III and,[54] $\frac{\partial \tau_{yGP}}{\partial c_{GP}}$ must be approximated due to its non-analytic dependence on GP zone diameter. For the Al-4 wt pct Cu alloy aged at 383 K (110 °C), $\tau_{yGP}(c_{GP})$ can be described reasonably well with a simple power law

$$\tau_{yGP} = \tau_{yGP}^0 c_{GP}^{3/7} \quad [D1]$$

with the fitting constant $\tau_{yGP}^0 = 1400$ MPa. Considering this relation and $\tau_{ys}/c_s^{2/3} = 1138$ MPa (from Section III), the inequality, $\frac{\partial \tau_{yGP}}{\partial c_{GP}} > \frac{\partial \tau_{ys}}{\partial c_s}$, implies that strength will increase as Cu atoms transfer from solute to GP zones if $c_{GP} < 0.663\ c_s^{7/12}$.

APPENDIX E: DERIVATION OF PLASTIC STRAIN RATE IN THE PRESENCE OF THERMAL ACTIVATION

First, the rate at which the controlling thermally activated events occur is assumed to follow an Arrhenius relation

$$\tilde{v} = \tilde{v}_0 exp\left(\frac{-\Delta E}{k_B T}\right). \quad [E1]$$

The exponential prefactor, $\tilde{v}_0$, is assumed to be a constant and the energy barrier, ΔE, is assumed to

only depend upon the ratio of the applied load, τ, over the load at which the thermally activated events occur instantaneously**, τ_{inst}. Assuming that

---

**We refer the interested reader to Nguyen et al.[89] for insight into the origin and significance of these assumptions.

---

the shape of the energy barrier, with respect to the reaction coordinate, is sinusoidal, the functional form of ΔE can be approximated to the first order as

$$\Delta E = \Delta E_0 \left(1 - \frac{\tau}{\tau_{\text{inst}}}\right)^{3/2}, \qquad [\text{E2}]$$

Finally, the rate at which the controlling thermally activated events occur, v, is assumed proportional to the plastic strain rate, $\dot{\gamma}$.

Assembling the above assumptions and Eqs. [E1] and [E2], one can construct a popular expression for relating the applied load τ to the plastic strain rate $\dot{\gamma}$ in the presence of thermal activation,[54,55]

$$\frac{\tau}{\tau_{\text{inst}}} = 1 - \left(\frac{k_{\text{B}}T}{\Delta E_0}\ln\frac{\dot{\gamma}_0}{\dot{\gamma}}\right)^{2/3}. \qquad [\text{E3}]$$

ELECTRONIC SUPPLEMENTARY MATERIAL

The online version of this article (doi: 10.1007/s11661-013-1614-1) contains supplementary material, which is available to authorized users.

REFERENCES

1. A. Wilm: *Metallurgie*, 1911, vol. 8, pp. 225–27.
2. F.W. Gayle and M. Goodway: *Science*, 1994, vol. 266, pp. 1015–17.
3. E. Orowan: *Z. Phys.*, 1934, vol. 89, p. 634.
4. M. Polanyi: *Z. Phys.*, 1934, vol. 89, p. 660.
5. G.I. Taylor: *Proc. R. Soc. Lond. A*, 1934, vol. 145, pp. 362–87.
6. A. Guinier: *Ann. Phys.*, 1939, vol. 12, p. 161.
7. G.D. Preston: *Phil. Mag.*, 1938, vol. 26, p. 855.
8. I. J. Polmear and H. K. Hardy: *J. Inst. Met.*, 1952–1953, vol. 81, pp. 427–32.
9. E. Hornbogen: *J. Light Met.*, 2001, vol. 1, pp. 127–32.
10. I. Polmear: *Light Alloys: From Traditional Alloys to Nanocrystals*, Butterworth-Heinemann, London, 2006.
11. P.V. Liddicoat, X.-Z. Liao, Y. Zhao, Y. Zhu, M.Y. Murashkin, E.J. Lavernia, R.Z. Valiev, and S.P. Ringer: *Nat. Commun.*, 2010, vol. 1, pp. 1–7.
12. R.Z. Valiev, N.A. Enikeev, Murashkin, V.U. Kazykhanov, and X. Sauvage: *Scripta Materialia*, 2010, vol. 63, pp. 949–52.
13. A. Guinier: *Heterogeneities in Solid Solutions, Vol. 9 of Solid State Physics*, Elsevier, Amsterdam, 1959, pp. 293–398.
14. K. Hono, T. Satoh, and K.-I. Hirano: *Philos. Mag. A*, 1986, vol. 53, pp. 495–504.
15. S.P. Ringer and K. Hono: *Mater. Charact.*, 2000, vol. 44, pp. 101–31.
16. M. Karlik, A. Bigot, B. Jouffrey, P. Auger, and S. Belliot: *Ultramicroscopy*, 2004, vol. 98, pp. 219–30.
17. J.M. Silcock, T.J. Heal, and H.K. Hardy: *J. Inst. Met.*, 1953–1954, vol. 82, pp. 239–48.
18. N.F. Mott and F.R.N. Nabarro: *Report on the Strength of Solids*, The Physical Society, London, 1948, p. 1.
19. V. Gerold and H. Haberkorn: *Phys. Stat. Solidi*, 1996, vol. 16, p. 675.
20. G. Knowles and P.M. Kelly: *BSC/ISI Conference, Scarborough*, The Iron and Steel Institute, London, 1971, p. 9.
21. E. Nembach: *Phys. Stat. Solidi (a)*, 1983, vol. 78, pp. 571–81.
22. P.B. Hirsch and A. Kelly: *Phil. Mag.*, 1965, vol. 12, p. 881.
23. A. Kelly and R.B. Nicholson: *Progr. Mater. Sci.*, 1963, vol. 10, pp. 151–91.
24. A. Kelly and M.E. Fine: *Acta Metallurgica*, 1957, vol. 5, pp. 365–67.
25. S.D. Harkness and J.J. Hren: *Metall. Trans. Am. Clin. Climatol. Assoc.*, 1970, vol. 1, pp. 43–49.
26. L.M. Brown and R.K. Ham: *Strengthening Methods in Crystals*, Applied Science Publishers, London, 1971, p. 9.
27. T. Eto: *Scripta Metallurgica*, 1980, vol. 14, p. 133.
28. S. Muraishi, N. Niwa, A. Maekawa, S. Kumai, and A. Sato: *Philos. Mag. A*, 2002, vol. 82, pp. 2755–71.
29. H. Van Swygenhoven and P.M. Derlet: *Phys. Revi. B*, 2001, vol. 64, pp. 224105–9.
30. S.I. Rao, T.A. Parthasarathy, D.M. Dimiduk, and P.M. Hazzledine: *Phil. Mag.*, 2004, vol. 84, pp. 3195–15.
31. M.P. Dewald and W.A. Curtin: *Modell. Simul. Mater. Sci. Eng.*, 2007, vol. 15, pp. 193–95.
32. T. Zhu, J. Li, A. Samanta, H.G. Kim, and S. Suresh: *PNAS*, 2007, vol. 104, pp. 3031–36.
33. Y.N. Osetsky and D.J. Bacon: *J. Nucl. Mater.*, 2003, vol. 323, pp. 268–80.
34. C. Kohler, P. Kizler, and S. Schmauder: *Model. Simul. Mater. Sci. Eng.*, 2005, vol. 13, pp. 35–45.
35. J.-H. Shim, Y.W. Cho, S.C. Kwon, W.W. Kim, and B.D. Wirth: *Appl. Phys. Lett.*, 2007, vol. 90, p. 021906.
36. D. Terentyev, G. Bonny, and L. Malerba: *Acta Metallurgica*, 2008, vol. 56, pp. 3229–35.
37. A. Takahashi and N.M. Ghoniem: *J. Mech. Phys. Solids*, 2008, vol. 56, pp. 1534–53.
38. C.V. Singh and D.H. Warner: *Acta Metallurgica*, 2010, vol. 58, pp. 5797–5805.
39. C.V. Singh, A. Mateos, and D.H. Warner: *Scripta Metallurgica*, 2011, vol. 64, pp. 398–401.
40. D.J. Bacon, Y.N. Osetsky, and D. Rodney: *Dislocation-Obstacle Interactions at the Atomic Level*, vol. 15, chap. 88, pp. 1–90, 2009.
41. H. Shercliff and M. Ashby: *Acta Metallurgica et Materialia*, 1990, vol. 38, pp. 1789–1802.
42. S. Schmauder and P. Binkele: *Comput. Mater. Sci.*, 2002, vol. 24, pp. 42–53.
43. M.J. Starink, N. Gao, L. Davin, J. Yan, and A. Cerezo: *Phil. Mag.*, 2005, vol. 85, pp. 1395–17.
44. G.E. Dieter: *Mechanical Metallurgy, Materials Science and Engineering*, 3rd ed., McGraw-Hill, New York, 1986.
45. D. Hull and D. Bacon: *Introduction to Dislocations*, 4th edn., Butterworth-Heinemann, London, 2001.
46. C. Kelchner, S. Plimpton, and J. Hamilton: *Phys. Rev. B*, 1998, vol. 58, pp. 11085–88.
47. J. Li: *Modell. Simul. Mater. Sci. Eng.*, 2003, vol. 11, pp. 173–77.
48. J. Friedel: *Les Dislocations*, Gauthier-Villars, Paris, 1956.
49. E. Orowan: *Symposium on Internal Stresses in Metals and Alloys*, Institute of Metals, London, 1984.
50. D.J. Bacon, U.F. Kocks, and R.O. Scattergood: *Phil. Mag.*, 1973, vol. 28, pp. 1241–63.
51. P.B. Hirsch: *J. Inst. Met.*, 1957, vol. 86, pp. 13–14.
52. T. Hatano: *Phys. Rev. B*, 2006, vol. 74, pp. 020102 + .
53. F.J. Humphreys and P.B. Hirsch: *Proc. R. Soc. Lond. A*, 1970, vol. 318, pp. 73–92.
54. G.P. Leyson, W.A. Curtin, L.G. Hector, and C.F. Woodward: *Nat. Mater.*, 2010, vol. 9, pp. 750–55.
55. R. Labusch: *Phys. Stat. Solidi (b)*, 1970, vol. 41, pp. 659–69.
56. R. Labusch: *Acta Metallurgica et Materialia*, 1972, vol. 20, pp. 917–27.
57. F. Apostol and Y. Mishin: *Phys. Rev. B*, 2011, vol. 83, p. 054116.
58. D. Olmsted, L. Hectorjr, and W. Curtin: *J. Mech. Phys. Solids*, 2006, vol. 4, pp. 1763–88.
59. C. Wolverton and V. Ozolins: *Phys. Revi. B*, 2006, vol. 73, p. 144104.
60. B. Diak and S. Saimoto: *Mater. Sci. Eng. A*, 1997, vol. 234 (236), pp. 1019–22.
61. S.A. Mousa, J. Bozarth, A. Youssef, B. Levine, B.J. Diak, K.R. Upadhyaya, and S. Saimoto: *Prog. Mater Sci.*, 1998, vol. 43, pp. 223–63.

62. A.J.E. Foreman and M.J. Makin: *Canad. J. Phys.*, 1967, vol. 45, pp. 511–17.
63. T. Nogaret and D. Rodney: *Phys. Rev. B*, 2006, vol. 74, pp. 134110+.
64. Z. Xu and R.C. Picu: *Phys. Rev. B*, 2007, vol. 76, pp. 094112+.
65. Y. Dong, T. Nogaret, and W.A. Curtin: *Metall. Mater. Trans. A*, 2010, vol. 41A, pp. 1954–60.
66. P. Binkele and S. Schmauder: *Z. Metallkd*, 2003, vol. 94, pp. 858–63.
67. G.I. Taylor: *J. Inst. Met.*, 1938, vol. 62, pp. 307–24.
68. G.I. Taylor: *Proceedings of the Colloquium on Deformation and Flow of Solids (Madrid, 1955)*, Springer, Berlin, 1956, pp. 3–12.
69. R.E. Stoller and S.J. Zinkle: *J. Nucl. Mater.*, 2000, vols. 283–287, pp. 349–52.
70. J. Wang, C. Wolverton, S. Muller, Z. Liu, and L. Chen: *Acta Materialia*, 2005, vol. 53, pp. 2759–64.
71. M. Avrami: *J. Chem. Phys.*, 1939, vol. 7, pp. 1103–12.
72. J. Christian: *The Theory of Phase Transformations in Metals and Alloys*, Pergamon Press, Oxford, 3rd edn., 2002.
73. E. Hornbogen: *Aluminum*, 1967, vol. 43, pp. 115–21.
74. T. Massalski: *J. Phase Equilib.*, 1980, vol. 1, pp. 27–33.
75. C. Wagner: *Z. Elektrochem.*, 1961, vol. 65, pp. 581–91.
76. J.F. Nie, B.C. Muddle, and I.J. Polmear: *Mater. Sci. Forum*, 1996, vols. 217–222, pp. 1257–62.
77. J. Yan: Ph.D. Thesis, School of Engineering Sciences, University of Southampton, 2006.
78. M. Starink: *Int. Mater. Rev.*, 2004, vol. 49, pp. 191–26.
79. J. W. Martin: *Precipitation Hardening*, Butterworth-Heinemann, London, 2nd edn., 1998.
80. C. Badini, F. Marino, and E. Verne: *Mater. Sci. Eng. A*, 1995, vol. 191, pp. 185–91.
81. G. Smith: *Thermochim. Acta*, 1998, vol. 317, pp. 7–23.
82. P. Bassani, E. Gariboldi, and G. Vimercati: *J. Therm. Anal. Calorim.*, 2007, vol. 87, pp. 247–53.
83. A. Ardell: *Metall. Trans. A*, 1985, vol. 16A, pp. 2131–65.
84. A. Argon: *Strengthening Mechanisms in Crystal Plasticity (Oxford Series on Materials Modelling)*, Oxford University Press, Oxford, 2007.
85. T. Hatano and H. Matsui: *Phys. Rev. B*, 2005, vol. 72, pp. 094105+.
86. H. Ney, R. Labusch, and P. Haasen: *Acta Metallurgica*, 1977, vol. 25, pp. 1257–69.
87. D.L. Olmsted, L.G. Hector, Jr., W. Curtin, and R. Clifton: *Modell. Simul. Mater. Sci. Eng.*, 2005, vol. 13, pp. 371–88.
88. J. Hirth and J. Lothe: *Theory of Dislocations*, McGraw-Hill, New York, 1968.
89. L. Nguyen, K. Baker, and D. Warner: *Phys. Rev. B*, 2011, vol. 2011 (84), p. 024118.
90. D.H. Warner, W.A. Curtin, and S. Qu: *Nat. Mater.*, 2007, vol. 6, pp. 876–81.
91. D. Warner and W. Curtin: *Acta Materialia*, 2009, vol. 57, pp. 4267–77.
92. D.R. Trinkle and C. Woodward: *Science*, 2005, vol. 310, pp. 1665–67.
93. S.J. Plimpton: *J. Comp. Phys.*, 1995, vol. 117, pp. 1–19.
94. M. S. Daw and M. I. Baskes: *Phys. Rev. B*, 1984, vol. 29, pp. 6443–53.
95. Y. Mishin, M. Mehl, and D. Papaconstantopoulos: *Acta Materialia*, 2005, vol. 53, pp. 4029–41.
96. E. Nembach and G. Neite: *Prog. Mat. Sci.*, 1985, vol. 29, pp. 177–319.